J. Fluid Mech. (2018), *vol.* 841, *pp.* 434–462.
doi:10.1017/jfm.2018.106

Condensates in rotating turbulent flows

Kannabiran Seshasayanan[1,†] **and Alexandros Alexakis**[1]

[1]Laboratoire de physique statistique, Département de physique de l' École normale supérieure, PSL Research University, Université Paris Diderot, Sorbonne Paris Cité, Sorbonne Universités, UPMC Univ. Paris 06, CNRS, 75005 Paris, France

(Received 12 July 2017; revised 16 January 2018; accepted 23 January 2018; first published online 23 February 2018)

Using a large number of numerical simulations we examine the steady state of rotating turbulent flows in triple periodic domains, varying the Rossby number Ro (that measures the inverse rotation rate) and the Reynolds number Re (that measures the strength of turbulence). The examined flows are sustained by either a helical or a non-helical Roberts force, that is invariant along the axis of rotation. The forcing acts at a wavenumber k_f such that $k_f L = 4$, where $2\pi L$ is the size of the domain. Different flow behaviours were obtained as the parameters are varied. Above a critical rotation rate the flow becomes quasi-two-dimensional and transfers energy to the largest scales of the system, forming large coherent structures known as condensates. We examine the behaviour of these condensates and their scaling properties close to and away from this critical rotation rate. Close to the critical rotation rate the system transitions supercritically to the condensate state, displaying a bimodal behaviour oscillating randomly between an incoherent-turbulent state and a condensate state. Away from the critical rotation rate, it is shown that two distinct mechanisms can saturate the growth of the large-scale energy. The first mechanism is due to viscous forces and is similar to the saturation mechanism observed for the inverse cascade in two-dimensional flows. The second mechanism is independent of viscosity and relies on the breaking of the two-dimensionalization condition of the rotating flow. The two mechanisms predict different scaling with respect to the control parameters of the system (Rossby and Reynolds), which are tested with the present results of the numerical simulations. A phase space diagram in the Re, Ro parameter plane is sketched.

Key words: rotating flows, rotating turbulence, turbulent flows

1. Introduction

Turbulent rotating flows are met in a variety of contexts in nature. From the interior of stars, to planet atmospheres and industrial applications, rotation plays a dominant role in determining the properties of the underlying turbulence (Greenspan 1968; Pedlosky 1987; Hopfinger & Heijst 1993). In its simplest form an incompressible turbulent flow in the presence of rotation is controlled by the incompressible Navier–Stokes equation, which in a rotating frame of reference reads

$$\partial_t \boldsymbol{u} + \boldsymbol{u}\cdot\boldsymbol{\nabla}\boldsymbol{u} + 2\Omega\hat{\boldsymbol{e}}_z \times \boldsymbol{u} = -\boldsymbol{\nabla}P + \nu\Delta\boldsymbol{u} + \boldsymbol{F}, \tag{1.1}$$

† Email address for correspondence: skannabiran@lps.ens.fr

where $\boldsymbol{u}$ is the incompressible velocity field, Ω is the rotation rate (assumed here to be in the z direction with $\hat{\boldsymbol{e}}_z$ its unit vector), P is the pressure that enforces the incompressibility condition $\boldsymbol{\nabla}\cdot\boldsymbol{u}=0$, ν is the viscosity and $\boldsymbol{F}$ is a mechanical body force that acts at some length scale ℓ_f. Traditionally, the strength of turbulence compared to viscous forces is measured by the Reynolds number $Re=U\ell_f/\nu$, while compared to the Coriolis force it is measured by the Rossby number $Ro=U/(2\Omega\ell_f)$, where U stands for the velocity amplitude. Precise definitions of these numbers will be given when we describe in detail the model under study.

It has been known for some time that when rotation is very strong, flows tend to become quasi-two-dimensional (quasi-2D) varying very weakly along the direction of rotation (Hough 1897; Proudman 1916; Taylor 1917). The reason for this behaviour is that the incompressible projection of the Coriolis force $2\Omega\hat{\boldsymbol{e}}_z\times\boldsymbol{u}-\boldsymbol{\nabla}P'=2\Omega\Delta^{-1}\partial_z\boldsymbol{\nabla}\times\boldsymbol{u}$ does not act on the part of the flow that is invariant along the rotation axis $\partial_z\boldsymbol{u}=0$. Here P' is the part of the pressure that enforces incompressibility condition for the Coriolis term and Δ^{-1} is the inverse laplacian. At the same time velocity fluctuations that vary along this axis become inertial waves that satisfy the dispersion relation,

$$\omega_{\boldsymbol{k}}=\pm 2\Omega\frac{k_z}{k}, \tag{1.2}$$

where $\omega_{\boldsymbol{k}}$ is the wave frequency, $\boldsymbol{k}$ the wavenumber and the sign depends on the helicity of the mode. Fast rotation leads to a de-correlation of inertial waves weakening their interactions. Thus, in the presence of strong rotation, fluid motions that are invariant along the direction of rotation (often referred as the slow manifold) become isolated from the remaining flow, and if forced they dominate, leading to the quasi-2D behaviour (Chen *et al.* 2005; Scott 2014). This quasi-2D behaviour has been realized in experiments (Ibbetson & Tritton 1975; Hopfinger, Browand & Gagne 1982; Dickinson & Long 1983; Baroud *et al.* 2002, 2003; Ruppert-Felsot *et al.* 2005; Sugihara, Migita & Honji 2005; Morize & Moisy 2006; Staplehurst, Davidson & Dalziel 2008; van Bokhoven *et al.* 2009; Yoshimatsu, Midorikawa & Kaneda 2011; Duran-Matute *et al.* 2013; Machicoane, Moisy & Cortet 2016) and numerical simulations (Yeung & Zhou 1998; Godeferd & Lollini 1999; Smith & Waleffe 1999; Chen *et al.* 2005; Mininni, Alexakis & Pouquet 2009; Thiele & Müller 2009; Favier, Godeferd & Cambon 2010; Mininni & Pouquet 2010; Sen *et al.* 2012; Marino *et al.* 2013; Alexakis 2015; Biferale *et al.* 2016; Valente & Dallas 2017).

These arguments, however, have various limitations. For large Reynolds numbers Re, the quasi-2D behaviour breaks down at scales ℓ smaller than the Zeman–Hopfinger scale ℓ_Z defined as the scale for which the vorticity $w_\ell\propto u_\ell/\ell$ is comparable to the rotation rate Ω (Hopfinger *et al.* 1982; Zeman 1994). Here u_ℓ stands for the typical velocity at scale ℓ. Thus, for large-Reynolds-number and low-Rossby-number flows, such that $1\ll 1/Ro\ll Re$, the large scales $\ell>\ell_Z$ show a quasi-2D behaviour, while smaller scales $\ell<\ell_Z$ display three-dimensional (3D) behaviour. Furthermore, the quasi-2D behaviour is also expected to break down even at large scales for sufficiently elongated boxes $H\gg\ell_f$, (where H stands for the domain size in the direction of rotation). If H is sufficiently large, the slowest inertial mode has a frequency $\omega\sim\Omega\ell_f/H$ comparable to or smaller than the inverse of the eddy turnover time ℓ/u_ℓ. This last limiting procedure, $1\ll 1/Ro\ll H/\ell_f$ provided also that $Re\gg 1$, corresponds to the weak wave turbulence limit, in which the nonlinear interactions can be treated in a perturbative manner (Galtier 2003; Nazarenko 2011). Finally, for finite (fixed) heights H and finite (fixed) Reynolds numbers, fast rotating flows become exactly 2D above a critical rotation rate (Gallet 2015). This corresponds to

the limiting procedure $Re \ll 1/Ro$ and $H/\ell_f \ll 1/Ro$. Thus, in general, the quasi-2D behaviour at low Ro depends on the scales under investigation, the geometry of the system, and the relative amplitude of the Rossby and Reynolds number, with different limits leading to different results.

The distinctive difference between 3D and 2D or quasi-2D flows is that the former cascades energy to small scales while the latter cascades energy to large scales. Thus a significant change in the energy balance occurs when the rotation rate is increased and the flow becomes quasi-2D: while in a forward cascade the energy that arrives at small scales gets dissipated, in an inverse cascade the energy piles up at scales of the size of the domain size L. Indeed, it has been shown both in numerical simulations (Smith, Chasnov & Waleffe 1996; Smith & Waleffe 1999; Sen *et al.* 2012; Pouquet *et al.* 2013; Deusebio *et al.* 2014; Biferale *et al.* 2016) and experiments (Duran-Matute *et al.* 2013; Yarom, Vardi & Sharon 2013; Campagne *et al.* 2014; Yarom & Sharon 2014; Campagne *et al.* 2015, 2016) that while for weak rotation the flow is close to an isotropic state and cascades all energy to the small scales, for fast rotation the flow is in a quasi-2D state that cascades at least part of the energy to the large scales. This quasi-2D state has also been observed in buoyancy-driven systems such as rotating convection (Favier, Silvers & Proctor 2014; Guervilly, Hughes & Jones 2014; Rubio *et al.* 2014; Stellmach *et al.* 2014; Kunnen *et al.* 2016; Plumley *et al.* 2016). This change in the direction of the cascade as a parameter is varied has been the subject of study of various investigations in different systems (Smith & Waleffe 1999; Celani, Musacchio & Vincenzi 2010; Alexakis 2011; Marino *et al.* 2013; Pouquet & Marino 2013; Deusebio *et al.* 2014; Seshasayanan, Benavides & Alexakis 2014; Marino, Pouquet & Rosenberg 2015; Sozza *et al.* 2015; Seshasayanan & Alexakis 2016; Benavides & Alexakis 2017). In particular, for rotating flows, it has been shown that the transition from a forward to an inverse cascade happens at critical rotation Ω_c above which the flow starts to cascade part of the injected energy ϵ inversely at a rate ϵ_{inv}. The fraction of the rate that cascades inversely ϵ_{inv}/ϵ depends on the difference $\Omega - \Omega_c$ and the height of the domain H (Deusebio *et al.* 2014). This description holds at early times before the inverse cascading energy reaches scales the size of the domain. At late times the energy starts to pile up at the largest scale of the system, altering the dynamics. This pile up of energy at the largest scale, amounting to a spectral condensation at the smallest wavenumbers, is referred in the literature as a condensate and has been the subject of many studies on 2D turbulence (Kraichnan 1967; Smith & Yakhot 1994; Xia *et al.* 2008).

In this work, we try to determine the behaviour of a forced rotating flow at late times when the flow has reached a steady state, in the absence of any large-scale dissipative mechanism. Due to the long computational time required to reach a steady state, very few investigations have focused on this regime like the early low-resolution studies in Bartello, Metais & Lesieur (1994) and, more recently, the studies in Alexakis (2015), Dallas & Tobias (2016), Yokoyama & Takaoka (2017), where turbulent rotating flows at steady state were investigated. Experiments on the other hand, for which long times are realizable, have investigated this steady-state limit (Duran-Matute *et al.* 2013; Campagne *et al.* 2014; Yarom & Sharon 2014; Campagne *et al.* 2016; Machicoane *et al.* 2016).

The rest of this paper is structured as follows. In § 2 we present our numerical set-up and introduce our control parameters and observables. In § 3 we discuss possible mechanisms for the saturation of the initial energy growth. In § 4 we present the results on global quantities from the numerical simulations and in § 5 we describe

the spatial and spectral structures as well the dynamics involved. In § 6 we discuss the effect of helicity of the forcing on the resulting flow. In § 7 we summarize and draw our conclusions.

2. Numerical set-up, and control parameters

We consider the flow of a unit density liquid in a cubic triple-periodic domain of size $2\pi L$ that is in a rotating frame with z being the axis of rotation. The governing equation for the flow velocity $\boldsymbol{u}$ is given by (1.1). The flow is driven by the body force $\boldsymbol{F}$; here we consider two cases given by

$$\boldsymbol{F} = f_0 \begin{bmatrix} -\sin(k_f y), \\ +\sin(k_f x), \\ \cos(k_f x) + \cos(k_f y) \end{bmatrix} \quad \text{and} \quad \boldsymbol{F} = f_0 \begin{bmatrix} -\sin(k_f y), \\ +\sin(k_f x), \\ \sin(k_f x) + \sin(k_f y) \end{bmatrix}. \tag{2.1a,b}$$

The first one is maximally helical $\langle \boldsymbol{F} \cdot \boldsymbol{\nabla} \times \boldsymbol{F} \rangle_S = \boldsymbol{k}_f \langle \boldsymbol{F} \cdot \boldsymbol{F} \rangle_S$ and will be referred to as the helical forcing and the second one has zero helicity $\langle \boldsymbol{F} \cdot \boldsymbol{\nabla} \times \boldsymbol{F} \rangle_S = \boldsymbol{0}$ and will be referred as the non-helical forcing. Here $\langle \rangle_S$ denotes spatial average. These forcing functions have been proposed by Roberts (1972) for dynamo studies and are commonly referred to as Roberts flow. Helicity, defined as $H = \langle \boldsymbol{u} \cdot \boldsymbol{\nabla} \times \boldsymbol{u} \rangle$, is known to play an important role in fast-rotating turbulence since it has been shown that its forward cascade can control the dynamics at the small scales (Mininni & Pouquet 2010; Sen *et al.* 2012). In this work we will examine both cases with and without helicity in parallel. It is also important to note that our forcing is invariant along the axis of rotation, and thus the forcing acts only on the slow manifold (that consists of all the Fourier velocity modes for which $k_z = 0$). This is in contrast with the case examined in Alexakis (2015), Yokoyama & Takaoka (2017), where a Taylor–Green forcing was used that has zero average along the vertical direction. Thus, while the Taylor–Green forcing does not inject energy directly to the slow manifold, the Roberts forcing used here injects energy only to the slow manifold. The two cases can thus be considered as two extremes.

This system was investigated using numerical simulations. All runs were performed using the pseudo-spectral code GHOST (Mininni *et al.* 2011), where each component of $\boldsymbol{u}$ is represented as a truncated Galerkin expansion in terms of the Fourier basis. The nonlinear terms are initially computed in physical space and then transformed to spectral space using fast Fourier transforms. Aliasing errors are removed using the 2/3 de-aliasing rule. The temporal integration was performed using a fourth-order Runge–Kutta method. Further details on the code can be found in Mininni *et al.* (2011). The grid size varied depending on the value of Re_F and Ro_F from 64^3 to 512^3. A run was considered well resolved if the value of enstrophy spectrum at the cutoff wavenumber was at least one order of magnitude smaller than its value at its peak. Each run started from a random multimode initial condition and was continued for a sufficiently long time that long-time averages in the steady state were obtained.

The parameter f_0 gives the amplitude of the forcing, and k_f is the wavenumber at which energy is injected into the flow. These two parameters define the length scale $\ell_f = k_f^{-1}$, the time scale $\tau_f = (k_f f_0)^{-1/2}$ and velocity amplitude $U_f = \sqrt{f_0/k_f}$ which will be used to non-dimensionalize the control parameters in our system. The product $k_f L$ gives the scale separation between the forcing scale and the box size. Throughout this work we have fixed the scale separation to $k_f L = 4$. We thus do not investigate the

dependence on the box size. The Reynolds number Re_f and the Rossby number Ro_f based on U_f are defined as

$$Re_f = \frac{\sqrt{f_0/k_f^3}}{\nu} \quad \text{and} \quad Ro_f = \frac{\sqrt{f_0 k_f}}{2\Omega}. \tag{2.2a,b}$$

The more classical definition of the Reynolds and Rossby number can be obtained using the root-mean-square amplitude of the velocity $U = \langle \boldsymbol{u} \cdot \boldsymbol{u} \rangle_{ST}^{1/2}$, where $\langle \cdot \rangle_{ST}$ denotes spatial and temporal average. This leads to the velocity based Reynolds number Re_u and the velocity based Rossby number Ro_u,

$$Re_u = \frac{U}{k_f \nu} \quad \text{and} \quad Ro_u = \frac{U k_f}{2\Omega}. \tag{2.3a,b}$$

In many experiments, as well as in many theoretical arguments, it is the energy injection rate

$$\epsilon = \langle \boldsymbol{u} \cdot \boldsymbol{F} \rangle_{ST} = \nu \langle |\boldsymbol{\nabla} \times \boldsymbol{u}|^2 \rangle_{ST} \tag{2.4}$$

per unit of volume that is controlled. It is thus worth expressing the control parameters also in terms of ϵ. This leads to the definition of the Reynolds/Rossby numbers based on ϵ,

$$Re_\epsilon = \frac{\epsilon^{1/3}}{\nu k_f^{4/3}} \quad \text{and} \quad Ro_\epsilon = \frac{\epsilon^{1/3} k_f^{2/3}}{2\Omega}. \tag{2.5a,b}$$

Finally, the ratio of the square root of enstrophy to twice the rotation rate is referred to as the micro-Rossby number Ro_λ, which in terms of Re_ϵ and Ro_ϵ can be expressed as

$$Ro_\lambda = \frac{\langle |\boldsymbol{\nabla} \times \boldsymbol{u}|^2 \rangle_{ST}^{1/2}}{2\Omega} = \frac{\epsilon^{1/2}}{2\nu^{1/2}\Omega} = Re_\epsilon^{1/2} Ro_\epsilon. \tag{2.6}$$

In the examined system only (Re_f, Ro_f) are true control parameters, while (Re_u, Ro_u) and $(Re_\epsilon, Ro_\epsilon)$ can only be measured *a posteriori*.

The location of all of the performed runs in the (Re_f, Ro_f) parameter space are shown in figure 1(*a*,*b*) for (*a*) helical flow and (*b*) non-helical flow in a log–log scale. The figure shows symbols that correspond to simulations that lead to different hydrodynamic steady states. Darker symbols correspond to larger values of Ro_f while larger symbols correspond to larger values of Re_f. The largest symbols correspond to simulation runs of size 512^3 points. The same symbols, sizes and shades (colours online) are used in some of the subsequent figures and thus the reader can refer to figure 1 to estimate the value of Re_f and Ro_f. Each symbol corresponds to different behaviour of the flow: squares ■ (red) correspond to flows that are laminar, diamonds ◆ (green) correspond to unstable or turbulent flows that do not form a condensate, and circles ● (black) correspond to turbulent flows that form a condensate. We have shifted the points corresponding to $\Omega = 0$, $Ro_f = \infty$ to the values $Ro_f = 100$ in order for them to appear along with other points that correspond to finite rotation.

The star symbols ⋆ (purple) denote the simulations of the reduced two-dimensional equations valid for $Ro_f \to 0$ given by

$$\left.\begin{aligned} \partial_t \boldsymbol{u}_{2D} + \boldsymbol{u}_{2D} \cdot \boldsymbol{\nabla} \boldsymbol{u}_{2D} &= -\boldsymbol{\nabla} p_{2D} + \nu \Delta \boldsymbol{u}_{2D} + \boldsymbol{f}_{2D}, \\ \partial_t \boldsymbol{u}_z + \boldsymbol{u}_{2D} \cdot \boldsymbol{\nabla} u_z &= +\nu \Delta u_z + \boldsymbol{f}_z, \end{aligned}\right\} \tag{2.7}$$

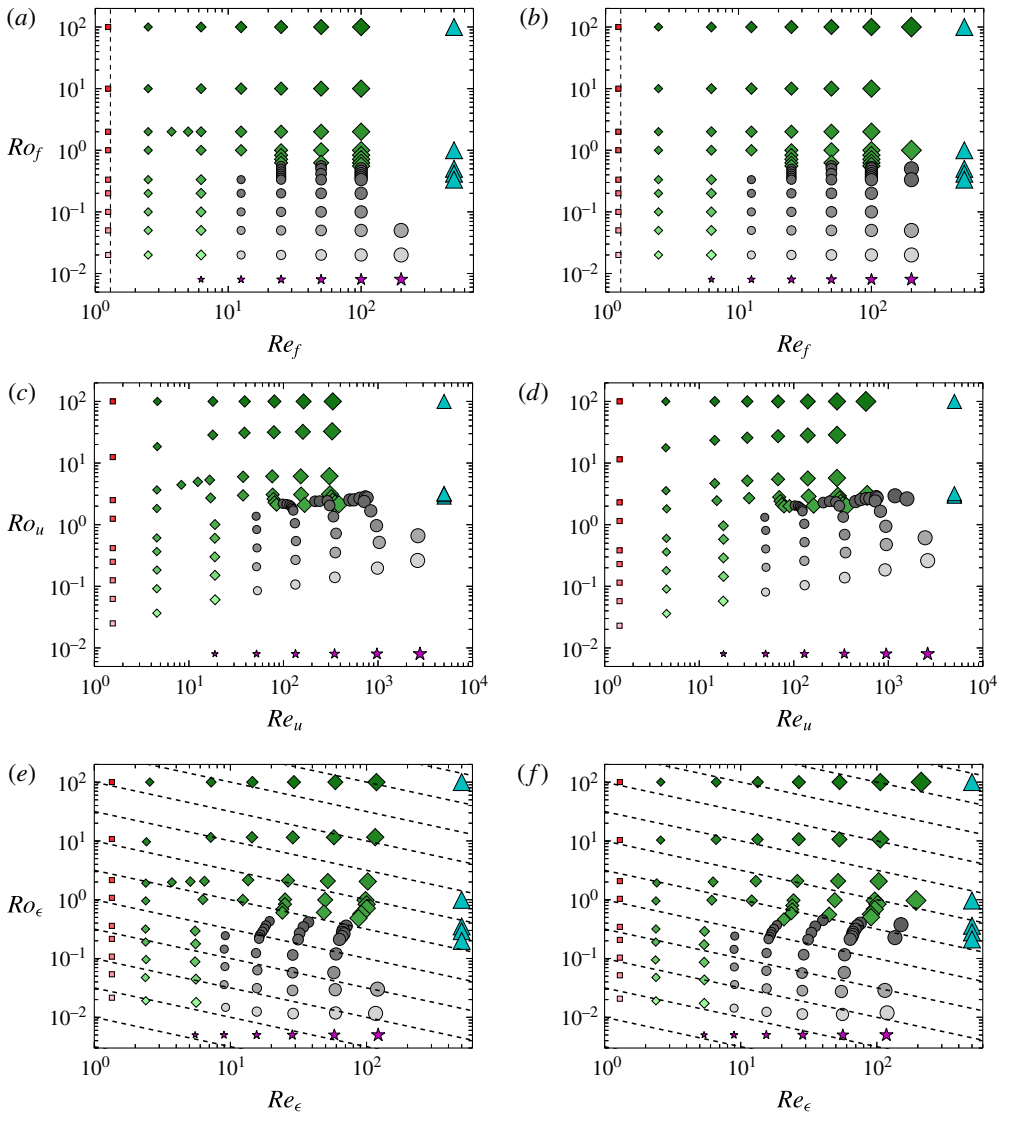

FIGURE 1. (Colour online) The figures show the location of the numerical runs in the (Ro_f, Re_f) parameter plane (*a*,*b*), the (Ro_u, Re_u) plane (*c*,*d*) and the $(Ro_\epsilon, Re_\epsilon)$ plane (*e*,*f*). Helical flows are in (*a*,*c*,*e*) and non-helical flows in (*b*,*d*,*f*). Larger symbols denote larger values of Re_f and lighter symbols correspond to smaller values of Ro_f. Different symbols correspond to different behaviour of the flow as follows: squares ■ (red) correspond to flows that are laminar, diamonds ◆ (green) correspond to unstable or turbulent flows that do not form a condensate, circles ● (black) correspond to turbulent flows that form a condensate, star symbols ⋆ (purple) denote the simulations of the reduced two-dimensional equations valid for $Ro_f \to 0$ and triangles ▲ (cyan) denote hyperviscous runs.

where $\boldsymbol{u}_{2D}$ stands for the horizontal components of the velocity field and u_z for the vertical. All fields are independent of the vertical coordinate z. The points for the 2D simulations ($Ro_f = 0$ limit) are placed at the position $Ro_f = 10^{-2}$. Finally, the triangles ▲ (cyan) denote hyperviscous runs obtained when we replace the Laplacian in (1.1)

with the Δ^4. Hyperviscous runs model the limit $Re_f \to \infty$ where a turbulent forward cascade is present. However, in systems like the present one, where inverse cascades build up, the hyperviscous dissipation could affect the amplitude of the large-scale condensate. This is why we only consider the results of hyperviscous runs along with DNS with regular viscosity. They are placed in figure 1 at the value $Re_f = 1000$.

The vertical dashed line stands for the linear stability boundary of the laminar flow. For the chosen forcing the first unstable mode is z-independent and is determined by the linearized version of (2.7). Accordingly the unstable mode is independent of rotation and the vertical component of the laminar flow. As a result the laminar stability boundary is independent of Ro_f and is the same for the helical and the non-helical flow, that share the same laminar $\boldsymbol{u}_{2D}$ at $Re_f \simeq 1.278$.

Figure 1(*c*,*d*) show the same points in the parameter plane (Re_u, Ro_u), with points in the parameter plane $(Re_\epsilon, Ro_\epsilon)$ shown in panels (*e*,*f*). The dashed lines in figure 1(*e*,*f*) indicate values of constant Ro_λ. For the range of examined parameters, compared to the points in the (Re_f, Ro_f) plane there is a clear shift of the points to larger values of Re_u as Ro_u is decreased in figure 1(*c*,*d*), while there is a decrease of Re_ϵ as Ro_ϵ is decreased in figure 1(*e*,*f*).

Our principal goal in this work is using this large number of numerical simulations to determine the dependence of the large-scale quantities of rotating turbulence such as the saturation amplitude U and the energy dissipation rate and to map the different behaviours observed in the parameter space making a phase space diagram.

3. Inverse transfers and saturation of condensates

In this section we present some theoretical estimates for the saturation amplitude of the velocity U and the energy dissipation rate ϵ. As a first step we consider a fixed energy injection rate ϵ and use $(Re_\epsilon, Ro_\epsilon)$ as control parameters. We relax this assumption later in the text, where we extend these considerations to the case of fixed forcing amplitude.

For weak rotating and non-rotating systems ($Ro \to \infty$) the cascade is strictly forward. The external forcing is balanced either by the viscous forces when Re is small, or by the nonlinearities that transfer the injected energy to the small scales where viscosity is again effective. These considerations lead to the classical scaling for laminar and turbulent flows between the velocity U and the energy injection rate ϵ,

$$U^2 \propto \epsilon \frac{\ell_f^2}{\nu} \quad \text{for } Re_\epsilon \to 0 \quad \text{and} \quad U^2 \propto (\epsilon \ell_f)^{2/3} \quad \text{for } Re_\epsilon \to \infty. \tag{3.1a,b}$$

Note that both of these scalings are independent of the domain size L and the rotation rate Ω. Using these scalings one can show that for $Re_\epsilon \to \infty$ all the definitions of Re given in the previous section are equivalent up to a prefactor so that $Re_\epsilon \sim Re_u \sim Re_f$ and $Ro_\epsilon \sim Ro_u \sim Ro_f$.

In the presence of an inverse cascade, however, the involved mechanisms for saturation become considerably different, altering these scaling relations. At late times, in order for the system to reach a steady state and saturate the initial increase of the large-scale energy, it has to either suppress the rate at which energy cascades inversely ϵ_{inv} or to reach sufficiently high amplitudes so that the energy can be dissipated by viscosity. If indeed the transition from forward to an inverse cascade

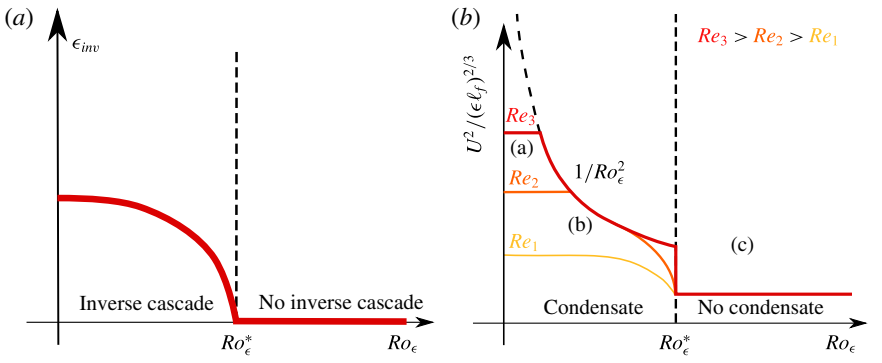

FIGURE 2. (Colour online) (*a*) Illustration of the expected dependence of the amplitude of the inverse flux ϵ_{inv} at the early stages of the inverse cascade as a function of the Rossby number Ro_ϵ. (*b*) Illustration of the expected total energy U^2 as a function of Ro_ϵ at the steady-state regime for different values of Re_ϵ. The dashed vertical line indicates the transition from a flow with no inverse cascade to a flow with an inverse cascade. The dashed curved line shows the scaling $1/Ro_\epsilon^2$ that reflects the $U^2 \propto \Omega^2 L^2$ scaling.

has a critical behaviour, the amplitude of the inverse cascade will depend as a power law on the deviation from criticality Ro_ϵ^*,

$$\epsilon_{inv} = C_1 \left(\frac{Ro_\epsilon^* - Ro_\epsilon}{Ro_\epsilon^*} \right)^\gamma \epsilon \quad \text{for } 0 < Ro_\epsilon^* - Ro_\epsilon \ll Ro_\epsilon^*, \tag{3.2}$$

while away from criticality it is expected that

$$\epsilon_{inv} = C_2\, \epsilon \quad \text{for } 0 < Ro_\epsilon \ll Ro_\epsilon^*. \tag{3.3}$$

Here Ro_ϵ^* denotes the critical value of Rossby for which the inverse cascade starts. Note that Ro_ϵ^* depends on the height of the box but not on the horizontal dimensions (see Deusebio *et al.* 2014). The result in (3.3) holds for the $Ro_\epsilon \to 0$ limit where the flow becomes 2D and ϵ_{inv} is independent of the rotation rate. The constant C_2 is unity when there is injection of energy only to the horizontal velocity components u_x, u_y, while it is between zero and one if u_z is forced, as is the case we examine here.

A sketch of the dependence of ϵ_{inv} on Ro_ϵ is shown in figure 2(*a*).

The prefactors C_1 and $C_2 \leqslant 1$ and the exponent γ have not yet been determined either by DNS or by experiments. In fact, even the conjecture of criticality is very hard to verify with DNS. Although it seems to be plausible, it has been demonstrated with some accuracy only for two-dimensional models (see Seshasayanan *et al.* 2014; Seshasayanan & Alexakis 2016; Benavides & Alexakis 2017). The reason is that close to the transition point, finite-size and finite-Reynolds effects become important that tend to smooth out the transition. To demonstrate this criticality, ever increasing box sizes and Reynolds numbers need to be considered, and this is extremely costly for three-dimensional simulations. We thus do expect that the transition might not appear as sharp as (3.2) might suggest and the results will be rather dominated by finite size effects that will smooth the transition.

For $Ro_\epsilon < Ro_\epsilon^*$ the energy that arrives at the domain size piles up, forming condensates. In rotating turbulence such condensates can saturate by two possible mechanisms. First, just like in the case of 2D turbulence, saturation comes from

viscous forces: the amplitude of the large-scale condensate U_{2D} becomes so big that viscous dissipation at large scale balances the rate ϵ_{inv} that energy arrives at the large scales by the inverse cascade. Thus, the balance $\epsilon_{inv} \propto \nu(U_{2D}^2/L^2)$ is reached. The scaling for the amplitude of the condensate close to the transition point Ro_ϵ^* thus follows,

$$U^2 \propto C_1 \frac{\epsilon L^2}{\nu} \left(\frac{Ro_\epsilon^* - Ro_\epsilon}{Ro_\epsilon^*} \right)^\gamma, \quad \text{for } 0 < Ro_\epsilon^* - Ro_\epsilon \ll Ro_\epsilon^*. \tag{3.4}$$

This argument indicates that if the injection rate ϵ is fixed, the amplitude of the condensate U scales supercritically with Ω with an exponent $\gamma/2$. For strong rotations away from criticality $Ro_\epsilon \ll Ro_\epsilon^*$, we expect the scaling for the condensate of 2D turbulence,

$$U^2 \propto C_2 \frac{\epsilon L^2}{\nu}, \quad \text{for } 0 < Ro_\epsilon \ll Ro_\epsilon^*. \tag{3.5}$$

We will refer to the condensate in this case as a viscous condensate because it is the viscosity that saturates the growth of energy at the large scales.

A different way to saturate the inverse cascade for fast-rotating flows is by breaking the conditions that make the flow quasi-2D. This can happen in domains with periodic boundary conditions, where due to the conservation of vorticity flux the shape of the condensate takes the form of a dipole with one co-rotating vortex and a counter-rotating vortex. Saturation of the inverse transfer of energy can then happen when the counter-rotating vortex cancels locally the rotation rate and energy cascades forward again (see Bartello *et al.* 1994; Alexakis 2015). This balance is achieved when the eddy turnover time of the condensate L/U becomes comparable to the rotation rate Ω. This leads to the scaling

$$U^2 \propto \Omega^2 L^2. \tag{3.6}$$

This scaling was realized in simulations of rotating Taylor–Green flows (see Alexakis 2015). Note that this scaling is independent of the amplitude of the inverse cascade, and thus independent of the deviation from criticality, that suggest that the transition will be subcritical. This was indeed found to be the case in Alexakis (2015). Furthermore, recently Yokoyama & Takaoka (2017) were able to follow the hysteresis diagram of the subcritical bifurcation. Finally, we also note that in this regime a strong asymmetry between co-rotating and counter-rotating vortices is expected, (see, for example, Hopfinger *et al.* 1982; Bartello *et al.* 1994; Morize & Moisy 2006; Bourouiba & Bartello 2007; Sreenivasan & Davidson 2008; Staplehurst *et al.* 2008; Van Bokhoven *et al.* 2008; Moisy *et al.* 2011; Gallet *et al.* 2014). We will refer to the condensate in this case as a rotating condensate because the energy at the large scales depends on the rotation rate.

From the two mechanisms the one that predicts a smaller value of U_{2D}^2 is going to be more effective. As the Rossby number Ro_ϵ is varied slightly below the critical value, we expect that due to the small amplitude of the inverse cascade, viscosity will be effective in saturating the inverse cascade and the saturation amplitude will be given by (3.4). Away from criticality, however, the breaking of the quasi-2D condition becomes more effective as the amplitude predicted by (3.6) will become smaller than (3.4), and the saturation amplitude will depend on rotation as in (3.6). The region for which the first scaling (3.4) holds becomes smaller as Re_ϵ increases. Thus, in the limit of large Re_ϵ the transition will become discontinuous. Viscosity will become effective again at very small Ro_ϵ where the saturation amplitude will be governed by

equation (3.5). The value of Ro_ϵ at which the behaviour transitions from the scaling (3.6) to the scaling (3.5) can be obtained by equating the two predictions. This leads to

$$Ro_\epsilon \propto Re_\epsilon^{-1/2}, \tag{3.7}$$

which implies that the transition from a rotating condensate to a viscous condensate occurs when the micro-Rossby number is of order unity $Ro_\lambda = O(1)$. As we will show in the coming sections, the difference between the two different saturation mechanisms is far from being limited to an abstract scaling. They result in considerable different structures and spectra (as will be shown later in figures 11 and 12).

Figure 2(*b*) shows a sketch of these expected transitions. The parameter space is thus split into three regions: Region (a), where a condensate forms that is balanced by viscosity for $Ro_\epsilon \ll Re_\epsilon^{-1/2} \ll Ro_\epsilon^*$, Region (b), in which the condensate that forms equilibrates to a steady state by the counter-rotating vortex cascading energy back to the small scales for $Re_\epsilon^{-1/2} \ll Ro_\epsilon < Ro_\epsilon^*$, and finally Region (c), where there is no inverse cascade and the system is close to isotropy for $Ro_\epsilon > Ro_\epsilon^*$. We stress that based on these arguments the behaviour of the flow at large Re_ϵ and low Ro_ϵ depends on the precise order in which the limits $Ro_\epsilon \to 0$ and $Re_\epsilon \to \infty$ are taken.

We now relax the assumption of fixed energy injection rate and consider the case where the system is forced by a constant-in-time forcing of fixed amplitude, as in our simulations. For weak rotation the relation between the forcing amplitude and energy injection rate if the Reynolds number is small is given by

$$\epsilon \propto \frac{f_0^2 \ell_f^2}{\nu} \quad \text{for } Re_f \ll 1, \quad \text{(laminar scaling)}, \tag{3.8}$$

while for large Reynolds numbers we have a viscosity-independent scaling:

$$\epsilon \propto f_0^{3/2} \ell_f^{1/2} \quad \text{for } Re_f \gg 1, \quad \text{(turbulent scaling)}. \tag{3.9}$$

For high rotation rates, however, the injection rate can depend on Ω if the forcing is not invariant along the axis of rotation. This was shown for the Taylor–Green forcing, where the flow was shown to re-laminarize at high rotation rates (Alexakis 2015). This effect will not take place in the present investigation, for which the forcing is z independent and we thus expect that the scaling in (3.9) remains valid, that along with (3.5) leads to the prediction

$$U^2 \propto U_f^2 Re_f (k_f L)^2 \quad \text{for } Ro_f \ll 1, \tag{3.10}$$

for the amplitude of the condensate. We note that in the presence of large-scale separation this relation is altered to the weaker scaling $U^2 \propto U_f^2 Re_f^{2/3} (k_f L)^{4/3}$ due to the effect of sweeping (see Shats *et al.* 2007; Xia *et al.* 2008; Tsang & Young 2009; Gallet & Young 2013). Such an effect, however, is not expected to be present in our case, for which $k_f L = 4$. For moderate values of Ro_f, such that the saturation comes from the cancelling of the quasi-2D condition of the counter-rotating vortex, U^2 is independent of the energy injection rate and thus from the forcing amplitude. U^2 is then given by (3.6). Thus, a qualitative difference between the constant injection of energy and constant forcing amplitude is only expected for viscous condensates, and only alters the dependence of the saturation amplitude on Re_f and not on Ro_f.

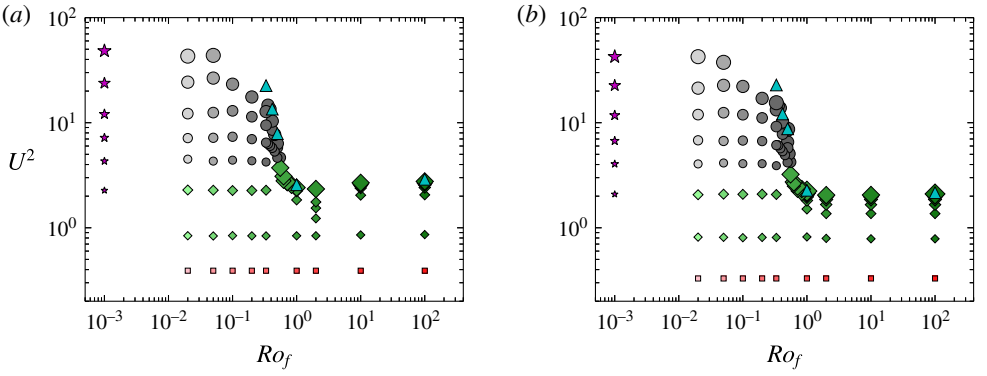

FIGURE 3. (Colour online) The figures show the total energy U^2 (in units of U_f^2) as a function of Ro_f for the examined numerical runs for (*a*) helical flow and (*b*) non-helical flow. Larger symbols denote larger values of Re_f and lighter symbols correspond to smaller values of Ro_f. Different symbols correspond to different behaviour of the flow as indicated in figure 1.

4. Simulation results

We begin by plotting in figure 3 the square of the velocity saturation amplitude U^2 (in units of U_f^2) as a function of the Rossby number for the entirety of our data points for the helical (*a*) and the non-helical (*b*) runs. For both cases the velocity amplitude increases rapidly as Ro_f decreases beyond a critical value $Ro_f^* = O(1)$. This increase appears to become stronger for larger values of Re_f (larger symbols). For larger values of Ro_f (weakly rotating runs), U_f^2 quickly saturates to a Ro_f- and Re_f-independent value provided Re_f is sufficiently above the laminar instability threshold.

As we show in what follows, the large increase of U^2 is due to the formation of a condensate at large scales. This is clear for large Re_f and strong rotation, where Ro_f is much smaller than the critical value. However, for values of the rotation close to the critical value Ro_f^* or for small Re_f, for which the condensate does not obtain such large values, a better indicator for a condensate formation is the energy U_{2D}^2 contained in the largest Fourier mode $|\boldsymbol{k}| = 1$, or in terms of the energy spectrum E_k we have $U_{2D}^2 = E(k = 1)$, where

$$E(k) = \left\langle \int |\hat{\boldsymbol{u}}(\boldsymbol{q})|^2 \delta(|\boldsymbol{q}| - k)\, \mathrm{d}q^3 \right\rangle \quad \text{with } \hat{\boldsymbol{u}}(\boldsymbol{q}) \equiv \frac{1}{(2\pi)^{3/2}} \int \boldsymbol{u}\, \mathrm{e}^{\mathrm{i}\boldsymbol{q}\cdot\boldsymbol{x}}\, \mathrm{d}x^3. \tag{4.1}$$

Figure 4 shows U_{2D}^2 as a function of Ro_f for a few different values of Re_f for helical and non-helical flow. From this figure the critical value Ro_f^* is estimated to be $Ro_f^* \simeq 0.6$ for both flows. The value of Ro_f^* is denoted by a vertical dashed line in the figures. For values above Ro_f^* the large-scale energy remains close to zero. Below Ro_f^* the energy U_{2D}^2 increases as Ro_f decreases further from Ro_f^* and asymptotes to a finite value as $Ro_f \to 0$ is approached.

Close to the onset the transition to the condensate appears to be supercritical, and U_{2D}^2 can be fitted to a function of the form $U_{2D}^2 \propto C_3(Ro_f^* - Ro_f)^\gamma$. From the present data we cannot measure with any significant accuracy the exponent γ. We note that increasing Re_f increases the saturation amplitude of U_{2D}^2, indicating that the prefactor C_3 depends on the Reynolds number. But in the large-Re_f limit, we see that the data

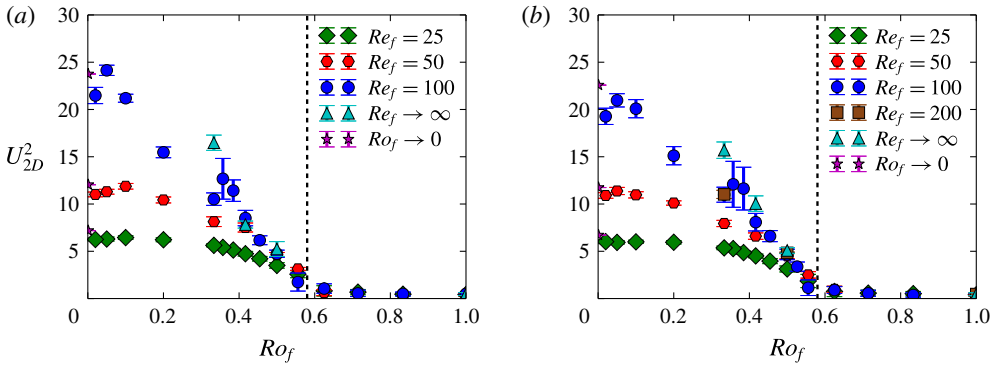

FIGURE 4. (Colour online) The figures show the energy at large scales U_{2D}^2 as a function of Ro_f (in units of U_f^2) for a few different values of Re_f for (*a*) helical flow and (*b*) non-helical flow. The vertical dashed line at $Ro_f \sim 0.6$ denotes the critical Rossby number Ro_f^* at which the system transitions to a condensate.

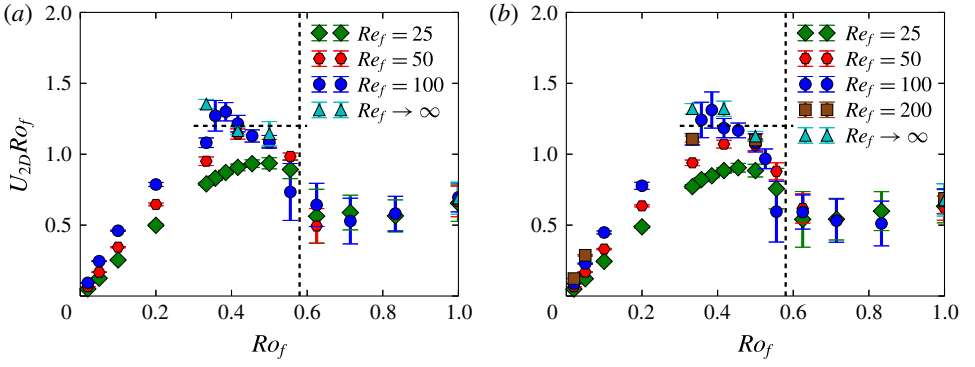

FIGURE 5. (Colour online) The figures show the product $U_{2D}Ro_f$ (in units of U_f) as a function of Ro_f for a few different values of Re_f for (*a*) helical flow and (*b*) non-helical flow. The vertical dashed line at $Ro_f \sim 0.6$ denotes the critical Rossby number for the transition to condensates. The horizontal dashed line denotes the scaling $U_{2D}Ro_f \sim 1$.

points converge for Ro_f close to Ro_f^*. This shows that, unlike the discussion in § 3 and the results of Alexakis (2015) and Yokoyama & Takaoka (2017), the transition at large Re_f is supercritical.

For intermediate values of Ro_f and for sufficiently large values of Re_f, we are expecting that U_{2D}^2 will saturate to values that follow the scaling of the rotating condensates $U_{2D} \propto \Omega L$ (3.6), that implies that the saturation amplitude is such that $U_{2D}Ro_f \simeq 1$. To test this expectation in figure 5 we plot $U_{2D}Ro_f$ as a function of Ro_f for different values of Re_f. Indeed in the region $0.3 > Ro_f > Ro_f^*$ the product $U_{2D}Ro_f$ appears to converge to an order one value as Re_f is increased, independent of Ro_f. We note that the largest Re_f points are close to the hyperviscous results, implying independence on Re_f has been reached. Although the results indicate that the saturation mechanism leading to (3.6) is plausible, the range of validity is too small to claim that the scaling has been demonstrated.

To extend the range of validity to smaller values of Ro_f we need to extend our simulations to larger values of Re_f. However, this becomes numerically very costly,

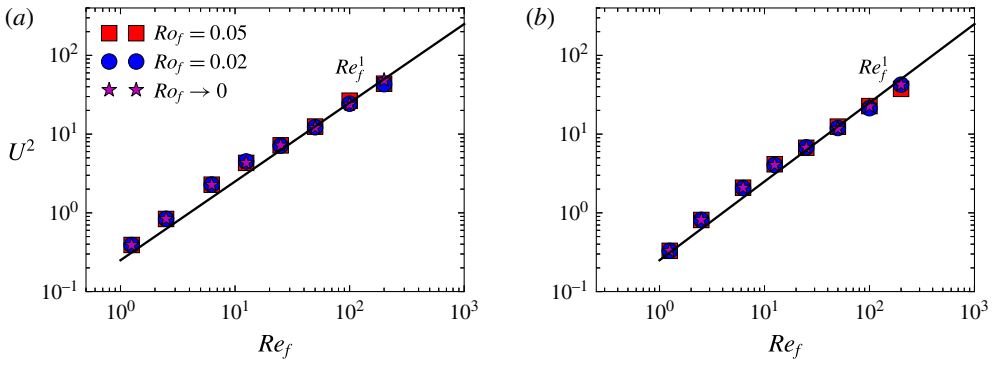

FIGURE 6. (Colour online) The figures show the energy U^2 (in units of U_f^2) as a function of Re_f for very small values of $Ro_f \ll 1$ for (a) helical flow and (b) non-helical flow. The thick line denotes the linear scaling with Re_f.

not only because it implies an increase of resolution, but also because the saturation amplitude of the condensate becomes large, and the time scale to reach saturation increases. As an example we mention that if we would like to extend the range of the rotating condensate to a value of Ro_ϵ half as small, it will require achieving a Re_ϵ that is four times as large as the one used now. This would require a spatial grid that is $4^{3/4}$ finer in each direction. If we take in to account the computational cost increase due to the CFL condition (Courant, Friedrichs & Lewy 1928) by a factor of $2 \times 4^{3/4}$ (due to the finer grid and twice larger U) and the twice longer duration of the run to attain saturation, we arrive at a computational cost that is 2^8 times more expensive than the present computations.

Finally, in figure 4, for very small values of Ro_f the energy U_{2D}^2 asymptotes to a finite value. This value matches the results obtained from the 2D simulations using equation (2.7) that are marked by a star, indicating that the flow has become two-dimensional. The saturation amplitude U_{2D}^2 at the $Ro_f \to 0$ limit, however, depends on the value of Re. In figure 6 we plot U^2 for the smallest values of Ro_f examined as a function of Re_f, along with the results from the system (2.7). The data scale linearly with Re_f in agreement with the prediction given in (3.10) for the viscous condensate. Equating the two results shown in figures 5 and 6, we obtain that the transition from the rotating condensate regime to the viscous condensate regime occurs when $Ro_f^{-2} \sim Re_f$, as seen in (3.7).

We now focus on the effect of rotation on the energy injection rate in the system. In figure 7 we plot the energy injection rate ϵ (in units of $f_0^{3/2} k_f^{1/2}$) as a function of Ro_f for the entirety of our data points for the helical (a) and the non-helical (b) runs. We remind the reader that smaller symbols indicate smaller Reynolds numbers as in figure 1. The energy dissipation rate saturates to a value independent of Re_f in the large-Re_f limit. This value, however, is different for small and large values of Ro_f, with the transition occurring over a thin region close to $Ro_f = Ro_f^*$. This is seen more clearly in figure 8, where we have concentrated on the five largest values of Re_f and plotted the data in a linear scale close to Ro_f^*. For these values of Re_f, the energy injection rate is decreased by a factor of five as Ro_f is decreased. The decrease in the value of ϵ as Ro_f is decreased occurs very fast when Ro_f is close to its critical value $Ro_f^* = 0.6$. The transition by this sudden jump at Ro_f^* indicates that, possibly close to the critical point, the dependence of ϵ on Ro_f could

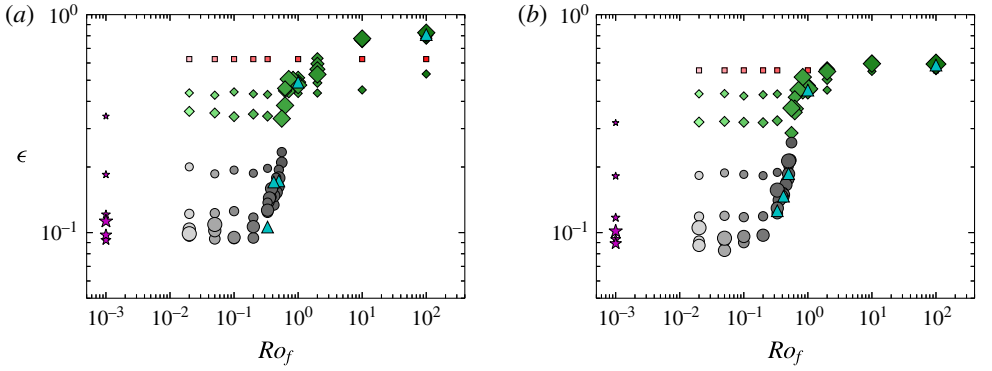

FIGURE 7. (Colour online) The figures show the injection/dissipation rate ϵ (in units of $U_f^3 k_f$) as a function of Ro_f for the examined numerical runs for (*a*) helical flow and (*b*) non-helical flow. Larger symbols denote larger values of Re_f and lighter symbols correspond to smaller values of Ro_f. Different symbols correspond to different behaviour of the flow as indicated in figure 1.

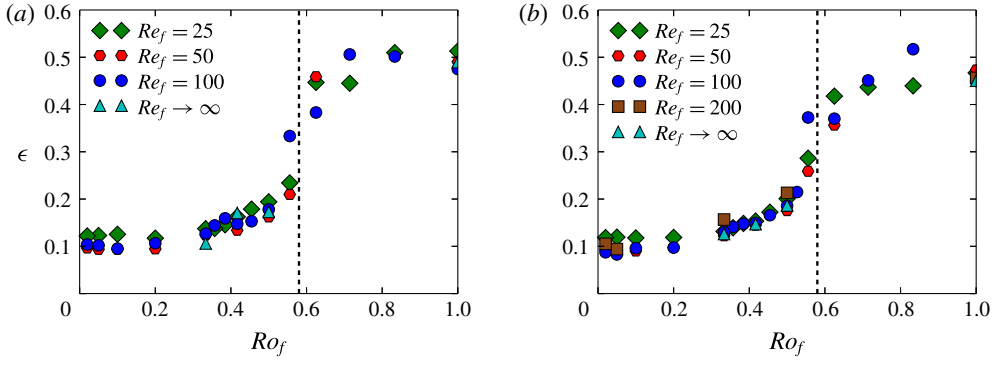

FIGURE 8. (Colour online) The figures show the dissipation rate ϵ (in units of $U_f^3 k_f$) as a function of Ro_f for a few different values of Re_f for (*a*) helical flow and (*b*) non-helical flow. The vertical dashed line at $Ro_f \sim 0.6$ denotes the critical Rossby number for the transition to a condensate.

be discontinuous. Another possibility is that ϵ is continuous but with diverging derivatives close to the critical point. Similar behaviour has been observed close to the transition to an inverse cascade for a two-dimensional magnetohydrodynamic flow where the low dimensionality of the system allowed a much closer investigation. In any case the investigation of the energy injection close to the critical rotation rate is very interesting but would require long runs that are expensive for numerical simulations but could be addressed more easily with experiments.

We conclude this section by considering the ratio $\epsilon/(U^3 k_f)$. The quantity $\epsilon/(U^3 k_f)$ is sometimes referred to as the drag coefficient. For laminar flows it scales like $1/Re_u$, while it tends to a non-zero constant for strongly turbulent flows at large Re_u. The finite asymptotic value of this ratio at large Re_u gives one of the fundamental assumptions of turbulence theory, that of finite dissipation at the zero-viscosity limit. This has been clearly demonstrated in experiments of non-rotating turbulence and large-scale numerical simulations (see Sreenivasan 1984; Kaneda *et al.* 2003;

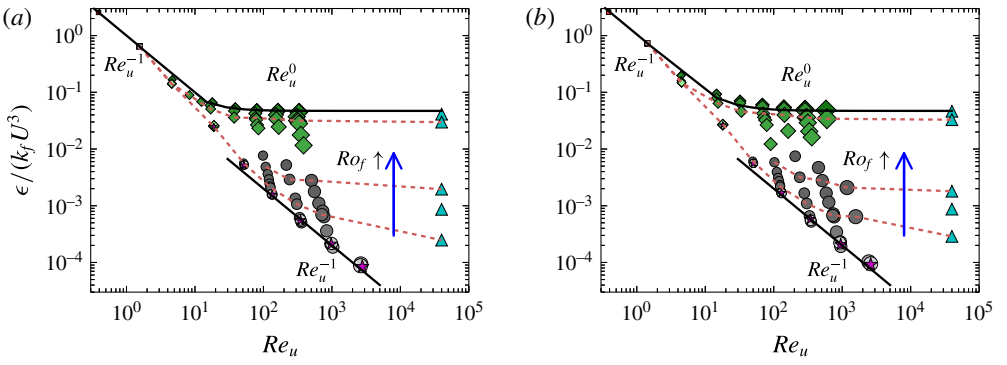

FIGURE 9. (Colour online) The figures show the normalized dissipation rate $\epsilon/(U^3 k_f)$ as a function of Re_u for the examined numerical runs for (*a*) helical flow and (*b*) non-helical flow. Larger symbols denote larger values of Re_f and lighter symbols correspond to smaller values of Ro_f. Different symbols correspond to different behaviour of the flow as indicated in figure 1. The thick lines denote the laminar scaling Re_u^{-1} and the turbulent scaling Re_u^0. The blue vertical arrow indicates the direction of increasing Ro_f (decreasing Ω). The three dashed brown lines connect the data points of three values $Ro_f = 1.0, 0.5, 0.33$ as we move from top to bottom.

Ishihara *et al.* 2016). In rotating turbulence experiments it has been investigated in Campagne *et al.* (2016), where the drag coefficient has been shown to scale as Ro_u for sufficiently small Ro_u. We note that in their experimental set-up it was the velocity of the propellers that were used to define Ro_u. In figure 9 we plot the ratio $\epsilon/(U^3 k_f)$ as a function of Re_u for different Rossby numbers. The arrow indicates the direction that Ro_f is increased (i.e. rotation is decreased). The dashed lines connect points with the same value of Ro_f for three different values of $Ro_f = 1.0, 0.5, 0.33$ as we move from top to bottom.

For rotation rates such that $Ro_f > Ro_f^*$ (diamonds), the data show a Re_u^{-1} scaling at low Re_u that transitions to a constant at large Re_u demonstrating a finite dissipation at infinite Re_u. This asymptotic value decreases slightly with Ro_f. For the runs with $Ro_f < Ro_f^*$ (circles) on the other hand, the region of the laminar scaling Re_u^{-1} appears to extend to larger values of Re_u. The very fast rotating runs (circles with light colours) and the $2D$ simulations from (2.7) show a Re_u^{-1} scaling throughout the examined range. The prefactor in front of Re_u^{-1} has decreased at the condensate regime because the laminar vortices are at the scale of the forcing (3.1) while the viscous condensate vortices are at the scale of the box size (3.5). However, for fixed Ro_f (dashed lines), as the Reynolds number is increased the Re_u^{-1} scaling appears to flatten to a Re_u-independent scaling. This occurs for the flows that are in the rotating condensate regime. This suggests that even for the rotating runs, the ratio $\epsilon/(U^3 k_f)$ will reach an asymptotic non-zero value at $Re_u \to \infty$ (for fixed Ro_f) matching the one obtained by the hyperviscous simulations. This asymptotic value, however, is different for different values of Ro_f, indicating that the value of the drag coefficient depends on the Rossby number.

The values of this asymptotic behaviour along with the results of the hyperviscous runs are shown in figure 10, where $\epsilon/(U^3 k_f)$ is plotted as a function of Ro_f. The results are compared with the scaling $\epsilon/(U^3 k_f) \propto Ro_f^3$. This scaling is obtained by assuming a constant injection rate and a saturation amplitude that follows $U \propto \Omega L$.

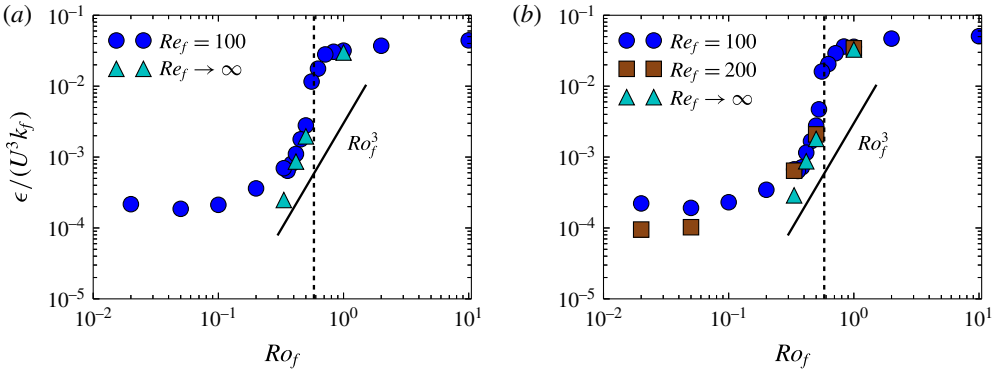

FIGURE 10. (Colour online) The figures show the normalized dissipation rate $\epsilon/(U^3 k_f)$ as a function of Ro_f for a few different values of $Re_f \gg 1$ for (*a*) helical flows and (*b*) non-helical flows. The thick line denotes the scaling Ro_f^3 and the vertical dashed line denotes the critical Rossby number for the transition to condensates.

The data appear to be slightly steeper. Perhaps this is not surprising considering the small range of Ro_f in which the scaling $U \propto \Omega L$ was shown to hold in figure 5. Note that weak wave turbulence predicts the scaling $\epsilon/(U^3 k_f) \propto Ro_\epsilon$, which is clearly not obtained here. We note also that the scaling $\epsilon/(U^3 k_f) \propto Ro$ was also obtained in the experiments of Campagne *et al.* (2016); however, not due to weak wave turbulence but due to a two-dimensionalization of the large-scale flow. The difference with the present scaling could be due to boundary layer effects that are absent in our simulations.

5. Structures, spectra and dynamical behaviour

In this section we try to obtain an understanding of the results in the previous section by visualizing the structures involved and examining their spectral and temporal behaviour. We start by the visualization of the flows. Figure 11 shows colour-coded visualizations of the vertical vorticity field. The red colours correspond to vorticity parallel to rotation while the blue colours correspond to vorticity antiparallel to rotation. The three images have been constructed from numerical simulations corresponding to the three regimes discussed in the previous section (in figure 2*b*)): panel (*a*) shows the viscous condensate, panel (*b*) shows the rotating condensate with the counter-rotating vortex cascading energy back to the small scales and (*c*) shows the weakly rotating (or non-rotating) turbulence. In the first case (panel *a*) the flow looks very close to a 2D state with no visible variations along the z direction and no observed asymmetry between co-rotating and counter-rotating vortices. In the second case (panel *b*) a condensate is also formed, but only clearly observed for the co-rotating vortex. The counter-rotating vortex, although present, is infested with small-scale eddies that extract energy from it. Finally, in the third case (panel *c*), no large-scale condensate is observed and the flow looks isotropic.

The spectra for the three cases are shown in figure 12. The spectrum for the flow in the viscous condensate regime is shown with a green dash-dot line. The energy is concentrated at the smallest wavenumber $kL = 1$, with the energy for wavenumbers above $k_f L = 4$ dropping very fast. In the non-rotating case, shown by a dashed line, energy is concentrated at the forcing wavenumber $k_f L = 4$ that is followed by a

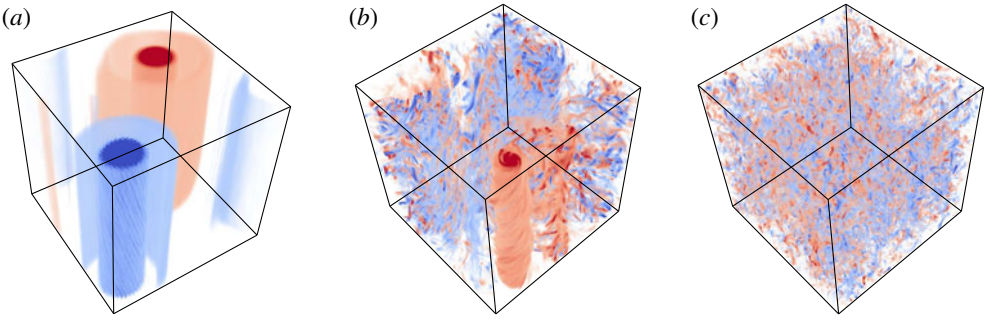

FIGURE 11. (Colour online) The figures show the contours of the vertical vorticity ω_z for (*a*) $Ro_f = 0.02$, $Re_f = 100$ (viscous condensate), (*b*) $Ro_f = 0.5$, $Re_f = 100$ (rotating condensate), (*c*) $Ro_f = \infty$, $Re_f = 100$ (3D turbulence). Red colours correspond to positive vorticity and blue colours correspond to negative vorticity.

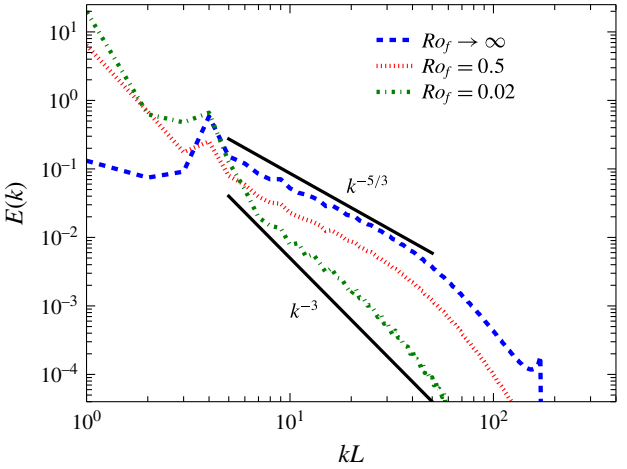

FIGURE 12. (Colour online) The figure shows the energy spectra for a few different values of Ro_f with $Re_f = 100$. The black thick lines denote the scaling $k^{-5/3}, k^{-3}$.

power-law spectrum close to $k^{-5/3}$. Finally, the case in the intermediate regime, shown by the dotted line, shows signs of both behaviours: the energy is concentrated at the largest scale $kL = 1$ as in the viscous condensate case but the spectrum at the small scales follows a $k^{-5/3}$ power law as in the non-rotating case. Thus, the spectrum for the rotating condensate is in agreement with the coexistence of a condensate along with a forward cascade. The temporal energy spectra in fast-rotating flows have been measured in experiments as well (see Duran-Matute *et al.* 2013; Campagne *et al.* 2015, 2016) although the different forcing mechanisms and absence of a Taylor hypothesis for the large scales makes it difficult to make a one-to-one comparison with the ones presented here. An obvious extension of the present work is the calculation of spatio-temporal spectra that allow one to make the connection between the two (di Leoni, Cobelli & Mininni 2015; Clark di Leoni & Mininni 2016).

The processes for upscale and downscale cascade are shown more clearly in figure 13, where the normalized energy flux $\Pi(k)/\epsilon$, the normalized 2D energy flux $\Pi_{2D}(k)/\epsilon$ and the normalized scale-dependent dissipation rate $D(k)/\epsilon$ are shown for

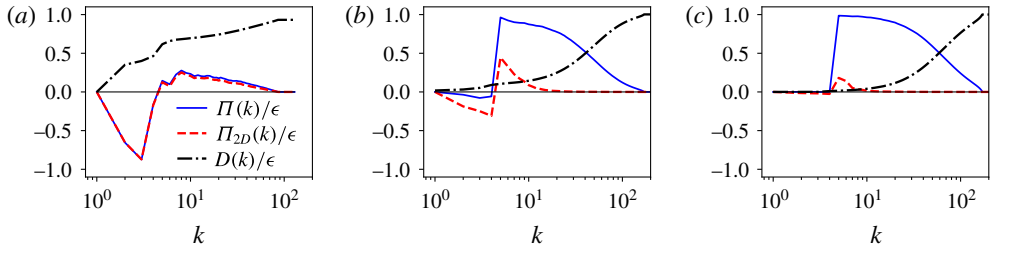

FIGURE 13. (Colour online) The figures show the normalized energy flux $\Pi(k)/\epsilon$, the normalized 2D energy flux $\Pi_{2D}(k)/\epsilon$ and the normalized scale-dependent dissipation rate $D(k)/\epsilon = \nu \sum_{|k'|<k}(k')^2 E(k')/\epsilon$ for three different cases, (*a*) viscous condensate $Ro_f = 0.02$, $Re_f = 100$, (*b*) rotating condensate $Ro_f = 0.5$, $Re_f = 100$ and (*c*) 3D turbulence $Ro_f = \infty$, $Re_f = 100$.

three different cases: figure 13(*a*) for the viscous condensate regime, figure 13(*b*) for the rotating condensate and figure 13(*c*) for 3D turbulent case with no rotation. The energy fluxes $\Pi(k)$, $\Pi_{2D}(k)$ and the scale-dependent dissipation rate $D(k)$ are defined as

$$\Pi(k) = \langle \boldsymbol{u}_k^< \cdot (\boldsymbol{u}\cdot\boldsymbol{\nabla}\boldsymbol{u})\rangle, \quad \Pi_{2D}(k) = \langle \overline{\boldsymbol{u}}_k^< \cdot (\overline{\boldsymbol{u}}\cdot\boldsymbol{\nabla}\overline{\boldsymbol{u}})\rangle, \quad D(k) = \nu \sum_{|k'|<k} (k')^2 E(k'), \quad (5.1a\text{–}c)$$

where $\boldsymbol{u}_k^<(x)$ stands for the filtered velocity so that only Fourier modes with wavenumbers of norm less than k are kept and the over-bar stands for vertical average. In the 3D-turbulence case, shown in figure 13(*c*), all the energy cascades to the small scales and the dissipation is concentrated at the smallest scales. In the rotating condensate, shown in figure 13(*b*), the 2D flux $\Pi_{2D}(k)$ is negative at large scales, indicating that the 2D motions transfer part of the energy to large scales sustaining the condensate. However, the net energy cascade to the large scales remains close to zero, as seen from $\Pi(k)$, implying that the remaining (not 2D) interactions bring the energy transferred to large scales by Π_{2D} back to the small scales in a flux loop mechanism. Similar flux loop mechanisms have been observed in 2D stratified turbulence (Boffetta *et al.* 2011) and compressible 2D turbulence (Falkovich & Kritsuk 2017). In this case the dissipation is seen to be concentrated at the small scales. Finally, in the case of the viscous condensate (figure 13*a*), the 2D flux $\Pi_{2D}(k)$ takes most of the energy to large scales, where it is dissipated. In the large scales the flux is negative and there is also a weak forward cascade to small scales, as seen from $\Pi(k)$, possibly related to the vertical velocity component whose related energy cascades forward. The total energy flux $\Pi(k)$ is almost identical to the 2D flux $\Pi_{2D}(k)$, implying that 3D effects are absent. The dissipation at the large scales is much larger than the previous cases, with more than half the total dissipation occurring at scales equal to and larger than the forcing scale.

We next examine the behaviour of the flow close to the transition point Ro_f^*. The arguments made in § 3 suggested that at large Re_f this transition would become discontinuous (subcritical), which was found for the Taylor–Green forcing (Alexakis 2015; Yokoyama & Takaoka 2017). The results in the previous section, however, showed that even at large Re_f the transition remains supercritical.

To understand this discrepancy, in figure 14(*a*) we show the time evolution of the total energy U^2 (lighter shade) and the energy of the large scales U_{2D}^2 for a value

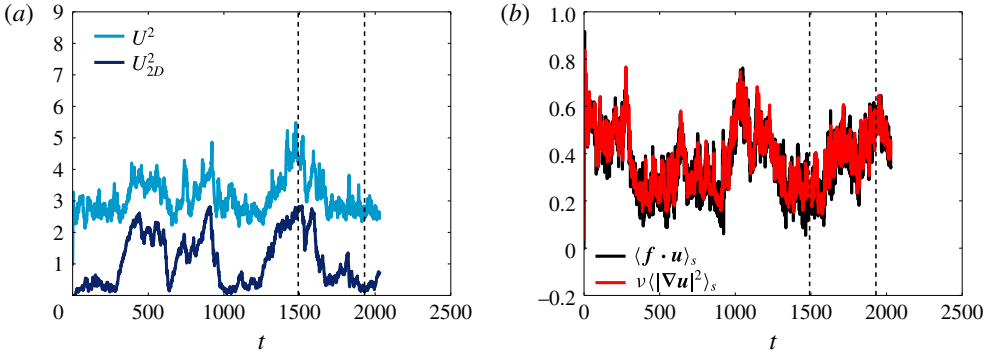

FIGURE 14. (Colour online) (*a*) Time series of the total energy U^2 and the energy at the large scales U_{2D}^2 for the case of $Ro_f = 0.556$, $Re_f = 100$, which is close to Ro_f^*. The vertical dashed lines denote the time instances at which the visualizations shown in figure 15 are taken. (*b*) Shows the spatial averaged energy injection rate $\langle \boldsymbol{f}\cdot\boldsymbol{u}\rangle_S$ and the dissipation rate $\nu\langle|\nabla\boldsymbol{u}|^2\rangle_S$ for the same run.

of $Ro_f = 0.556$ close to the critical value and a relatively large $Re_f = 100$. The flow randomly oscillates between two distinct states: one where the energy of the large scales is weak and most of the energy lies in the forcing scales, and one where the energy of the large scales dominates and accounts for more than 60 % of the total energy. The energy at the large scales varies by an order of magnitude between these two states with $U_{2D}^2 \sim \Omega^2 L^2$ when U_{2D}^2 dominates and $U_{2D}^2 \ll \Omega^2 L^2$ at its low values. In figure 14(*b*) the time series of the spatial-averaged energy injection rate $\langle \boldsymbol{f}\cdot\boldsymbol{u}\rangle_S$ and the energy dissipation rate $\nu\langle|\nabla\boldsymbol{u}|^2\rangle_S$ is shown. A burst of energy dissipation is observed at the time instances that the flow transitions from the condensate to the 3D turbulent state. This correlation between the change of state in the large scales and the energy dissipation/injection is typical of bimodal systems (Mishra *et al.* 2015). Visualizations of the vertical vorticity of the flow are shown in figure 15 at the two different times indicated by the vertical dashed lines in figure 14(*a*,*b*). The two figures resemble the ones shown in figure 11(*b*,*c*) that were obtained for different values of the parameter Ro_f.

It appears thus that the transition from isotropic turbulence to rotating condensate occurs through a bistable regime where both states are realized at different instances of time. The two states are distinct, i.e. they are separated by a finite amount of energy; however, the time the system spends in each one of these states can depend on the deviation from the onset Ro_f^*, becoming infinite for the condensate state for Ro_f sufficiently smaller than Ro_f^*. The time-averaged quantities displayed in the previous sections thus remain continuous. This bistable behaviour, if it persists at larger Re_f, will indicate that the transition will remain supercritical. Similar behaviour has been observed in experiments in a rotating tank where intermittent switching between blocked and large-scale zonal patterns has been observed Weeks *et al.* (1997). This presents an alternate mechanism other than the subcritical transition discussed in § 3 and observed in Alexakis (2015), Yokoyama & Takaoka (2017).

A similar oscillating behaviour is observed even further from the onset Ro_f^*. In figure 16(*a*) we show the time evolution of U_{2D}^2 and U^2, as in figure 14(*a*), for a slightly smaller value of $Ro_f = 0.357$. Unlike the previous case the system here is only in the condensate regime with the energy concentrated at the largest scale

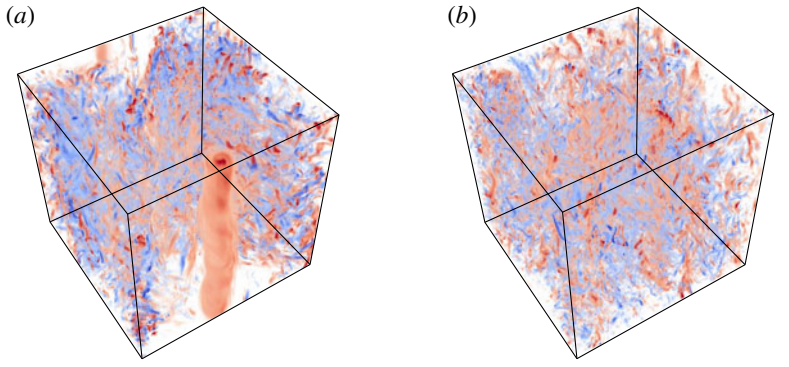

FIGURE 15. (Colour online) The figures show the contours of the vertical vorticity ω_z for $Ro_f = 0.556$, $Re_f = 100$ for the two time instances marked in figure 14(*a*). Red colours correspond to positive vorticity and blue colours correspond to negative vorticity. In panel (*a*) a co-rotating vortex is formed when the system is in the condensate regime, while panel (*b*) does not have any large-scale structure.

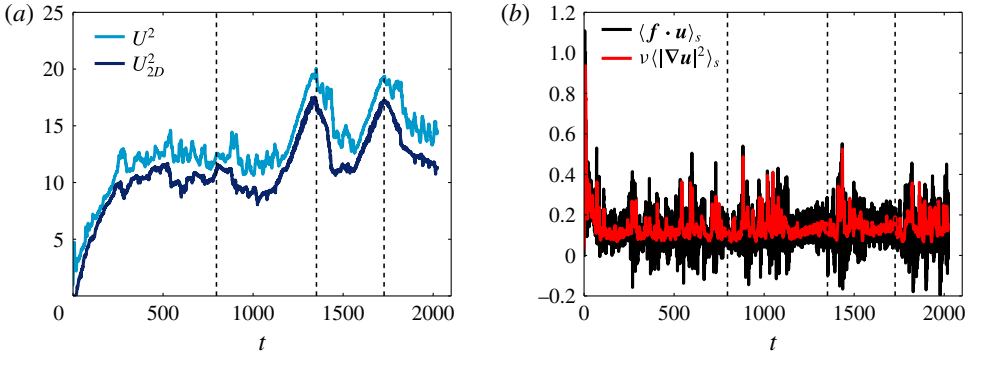

FIGURE 16. (Colour online) (*a*) The time series of the total energy U^2 and the energy at the large scales U_{2D}^2 for the case of $Ro_f = 0.357$, $Re_f = 100$, which is below Ro_f^*. The vertical dashed lines denote the time instances at which the visualizations shown in figure 17 are taken. (*b*) The spatial averaged energy injection rate $\langle \boldsymbol{f} \cdot \boldsymbol{u} \rangle_S$ and the dissipation rate $\nu \langle |\nabla \boldsymbol{u}|^2 \rangle_S$ for the same run.

$kL = 1$. U_{2D}^2 is always dominant and it undergoes strong fluctuations. Figure 16(*b*) shows the time series of the spatially averaged energy injection rate $\langle \boldsymbol{f} \cdot \boldsymbol{u} \rangle_S$ and the energy dissipation rate $\nu \langle |\nabla \boldsymbol{u}|^2 \rangle_S$ for the same run as figure 16(*a*). The peaks of energy injection/dissipation are correlated with changes in the large-scale flow states. We note that in the condensate regime, even though the dissipation is always positive, the energy injection rate takes both negative and positive values. This means that at certain instances of time the forcing takes energy out of the system. Visualization of the flows in figure 17 at different times reveal that these fluctuations correspond to a transition of the flow from a state that has a co-rotating vortex that is stable to states that are unstable to 3D fluctuations that, however, fail to destroy it. Thus, it seems that the key to understanding the behaviour of this flow lies in understanding the stability properties of these freely evolving vortices.

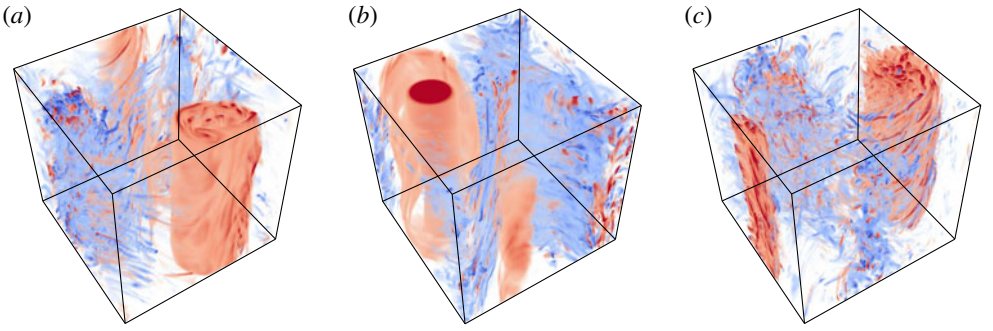

FIGURE 17. (Colour online) The figures show the contours of the vertical vorticity ω_z for $Ro_f = 0.357$, $Re_f = 100$ for the three time instances marked in figure 16(*a*). Red colours correspond to positive vorticity and blue colours correspond to negative vorticity.

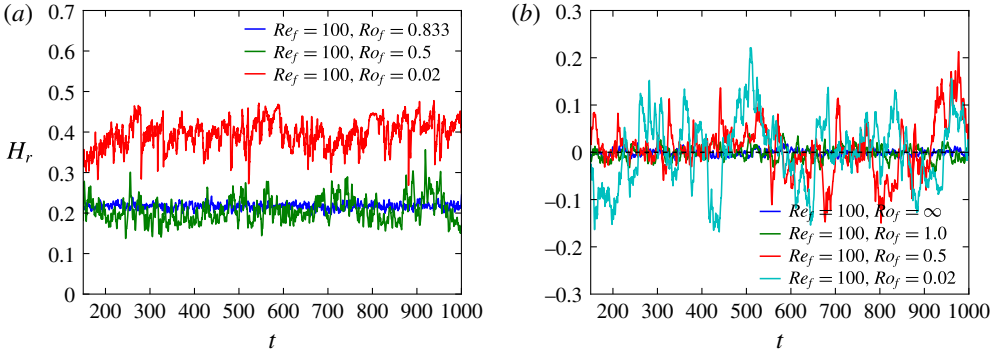

FIGURE 18. (Colour online) The figures show the time series of the relative helicity H_r as a function of time for a few different Rossby numbers and fixed $Re_f = 100.0$ for (*a*) helical runs and (*b*) non-helical runs.

6. Effect of helicity

Finally we comment on the effect of helicity on the condensate formation. Contrary to the small-scale behaviour, where the presence of helicity was shown to play a significant role (Mininni & Pouquet 2010; Sen *et al.* 2012), in the present investigation it was shown that it did not affect the dynamics of the observed large-scale quantities. Both helical and non-helical flows were shown to obey the same scaling laws, and only small variations were observed in the prefactors. This is perhaps not surprising since helicity cascades to the small scales, and thus it does not affect the large scales of the condensates.

In figure 18 we show the time series of the relative helicity H_r for a few different values of Ro_f and fixed $Re_f = 100$ for both the helical and the non-helical cases. The relative helicity is defined as

$$H_r = \frac{\langle \boldsymbol{u} \cdot \boldsymbol{\nabla} \times \boldsymbol{u} \rangle_S}{\langle |\boldsymbol{u}|^2 \rangle_S^{1/2} \langle |\boldsymbol{\nabla} \times \boldsymbol{u}|^2 \rangle_S^{1/2}}. \tag{6.1}$$

For the helical forcing case the relative helicity is always non-zero and increases as we reduce Ro_f. For the small values of Ro_f it reaches a value of approximately 0.4.

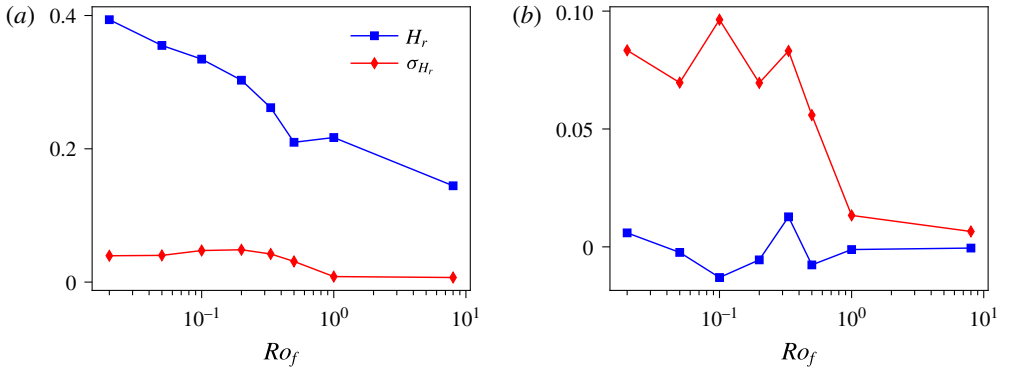

FIGURE 19. (Colour online) The figures show the relative helicity H_r and the standard deviation of the relative helicity σ_{H_r} as a function of Ro_f for fixed $Re_f = 100$ for (a) helical runs and (b) non-helical runs.

For the non-helical case the relative helicity oscillates around zero; however, with the fluctuations being significantly strong and larger for smaller values of Ro_f. It is also worth noting that the time scale of these fluctuations increases as the rotation becomes larger. This has already been observed in Dallas & Tobias (2016).

In figure 19 we show the time-averaged relative helicity H_r and the standard deviation of the relation helicity σ_{H_r} as a function of Ro_f for both helical and non-helical forcing with $Re_f = 100$. For the helical forcing, as Ro_f is decreased the relative helicity and the fluctuations increase. For the non-helical case, also the fluctuations increase when Ro_f is decreased below the critical value, even if the mean remains zero. The fluctuations in the mean helicity can play an important role for dynamo studies in turbulent rotating flows (see Seshasayanan, Dallas & Alexakis 2017).

7. Conclusions

This work gives a description of steady-state rotating turbulence when the forcing acts directly on the slow manifold, by mapping the parameter space with the different behaviours observed and the resulting scaling relations. Our results are concisely summarized in figure 20, where the four different phases of the rotating flows examined are shown in the parameter space (Re_f, Ro_f): laminar flow, 3D turbulence flow, rotating condensate flow and viscous condensate flow. Solid lines indicate the boundaries where a critical transition takes place, while dashed lines indicate smooth transitions.

For values of Re_f below a critical value Re_f^* that is independent of Ro_f, the flow has a laminar behaviour. At this state the resulting flow is 2D, independent of time, and proportional to the inverse Laplacian of the forcing. The first unstable mode in this laminar state is a 2D mode that is not affected by the rotation, and thus the instability boundary does not depend on Ro_f.

For $Re_f \gg Re_f^*$ and Ro_f above a critical value Ro_f^*, the flow displays quasi-isotropic 3D turbulence. This regime is described to a good degree by Kolmogorov–Richardson phenomenology (Richardson 1926; Kolmogorov 1941), and classical results of turbulence like the finite energy dissipation at the zero-viscosity limit and a $k^{-5/3}$ energy spectrum appear to hold.

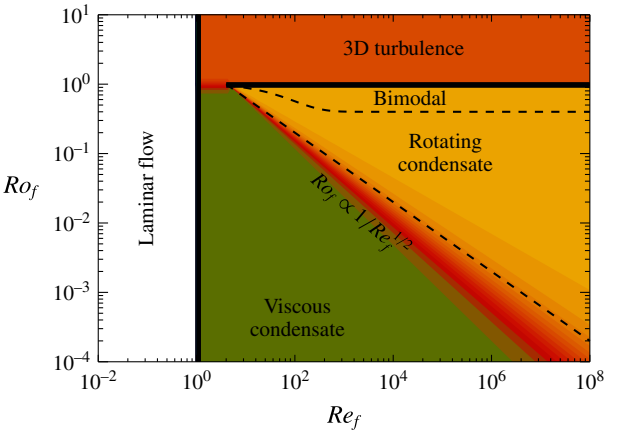

FIGURE 20. (Colour online) The figure shows the phase space diagram with the different flow behaviour marked. Solid lines denote sharp/critical transitions. Dashed line denotes smooth transitions.

For $Re_f \gg Re_f^*$ and $Re_f^{-1/2} \ll Ro_f \leqslant Ro_f^*$, the flow is shown to be in what we refer as a rotating condensate state. In this state a co-rotating 2D vortex is dominant at the large scales while the counter-rotating vortex breaks down to 3D eddies cascading energy back to the small scales. At this state the amplitude of the condensate U_{2D} (in the rather small range examined by our simulations) was shown to be proportional to the rotation rate $U_{2D} \propto \Omega L$. Our results also indicate (with the help of hyperviscous simulations) that in this regime the finite energy dissipation at the zero-viscosity limit still holds but with a drag coefficient that rapidly decreases with Ro_f. The spectra at the small scales follow a close to $k^{-5/3}$ power law, while a large peak appears at the largest scale, indicating the presence of the condensate.

The transition from the quasi-isotropic 3D turbulent state to the rotating condensate state was shown to be supercritical, contrary to the arguments described in the introduction that were predicting that at sufficiently large Re_f, right below criticality Ro_f^*, the system would transition discontinuously to the rotating condensate value $U_{2D}^2 \propto \Omega^2 L^2$. The reason for this discrepancy is in part because the arguments in § 3 assumed weak dependence of the energy injection rate ϵ at criticality, while the DNS showed a strong sensitivity of ϵ on Ro_f close to criticality. The second reason is that the system close to criticality showed a bimodal behaviour where part of the time was spent in the 3D turbulence state with $U_{2D}^2 \ll \Omega^2 L^2$ and the remaining part was spent in the rotating condensate state with $U_{2D}^2 \propto \Omega^2 L^2$. Despite the fact that these states have distinct energy levels, the time spent in the condensate state can decrease continuously to zero as $Ro_f \to Ro_f^*$ (from below), leading to a continuous supercritical transition.

For $Re_f \gg Re_f^*$ and $Ro_f \ll Re_f^{-1/2}$ the flow is shown to be in what we refer to as a viscous condensate state. In this state the flow is close to 2D and both the co-rotating and counter-rotating 2D vortices exist and dominate the large scales. The flow has a normalized energy dissipation rate that decreases with Re_u, following the laminar scaling Re_u^{-1}. The transition from the rotating condensate regime to the viscous condensate was found to be smooth. We note, however, that another critical value of Ro_f is expected for which the flow becomes exactly 2D and all 3D perturbations

decay exponentially (Gallet 2015). Such a transition is expected at even smaller values of Ro_f, and to observe it we have to focus on deviations from 2D flows, which was not done in the present study. A similar study in thin layers has shown that this transition is governed by strong intermittent events (Benavides & Alexakis 2017). Thus, this is an interesting limit that is worth investigating in the future.

The difference between the parameters (Re_f, Ro_f) and (Re_u, Ro_u) or (Re_ϵ, Ro_ϵ) was not found to be as severe as in the Taylor–Green flow, where discontinuous (subcritical) transitions were present, which results in mapping from one set of parameters to the other being neither one-to-one nor onto. In particular, the difference between (Re_f, Ro_f) and (Re_ϵ, Ro_ϵ) was only found to be significant close to the critical point Ro_f^* where ϵ was found to change abruptly. The difference between (Re_f, Ro_f) and (Re_u, Ro_u) was stronger, and is due to the fact that in the rotating condensate regime the scaling $U \propto \Omega L$ merged all values of Ro_u to be close to unity. This left all larger values of Ro_u to be in the viscous condensate regime. Thus, in the steady-state regime, at least Ro_u does not appear to be a good indicator for the strength of rotation.

We stress the importance of the ordering of the limits when one considers the low-Rossby-number, large-Reynolds-number limit. If one considers the $Ro_f \to 0$ limit first, and afterwards the $Re_f \to \infty$ limit then one always falls in the viscous condensate regime. While if one considers the $Re_f \to \infty$ first one falls in the rotating condensate regime. To distinguish between the two one needs to look at the products $Ro_f Re_f^{1/2}$ or $Ro_\lambda = Ro_\epsilon Re_\epsilon^{1/2}$. Referring thus to the large-Reynolds-number, small-Rossby-number limit is ambiguous unless the ordering is specified.

The presence or absence of helicity in the forcing does not affect the dynamics of the large-scale condensates. Both helical and non-helical forcing lead to similar bifurcation diagrams and scaling laws for the large-scale quantities. This perhaps could have been expected since helicity is a quantity that cascades to the small scales and is unlikely to affect the condensate scales. However, the normalized mean helicity did display non-trivial dynamics. Its mean value increased as Ro_f was decreased for the helical forcing case, while for the non-helical forcing even if the mean value was zero then strong fluctuations were present. In both cases the fluctuations of the relative helicity are stronger in the condensate regime.

We note that the results presented here are obtained in a cubic box. Varying box height gives rise to different values of Ro_f^*, as discussed in § 3 (see Deusebio *et al.* 2014). Also varying the box size in the horizontal direction with respect to the forcing length scale is something that has not been examined in our runs. Although we have concluded the scaling $U_{2D}^2 \sim \Omega^2 L^2$ for the amplitude of the condensate, we have only verified this scaling with rotation and not with the box size L. This is something that needs to be examined in future investigations. Furthermore, the presence of anisotropy in the two horizontal directions tends to alter the structure of the flow from vortex dipoles to shear layers, as has been suggested in Bouchet & Simonnet (2009), Bouchet & Venaille (2012) and shown recently for 2D turbulence (Frishman, Laurie & Falkovich 2017), and rapidly rotating convection (Guervilly & Hughes 2017; Julien, Knobloch & Plumley 2018) and this is a new direction where condensate dynamics could be studied.

Finally, we comment on the effect of boundaries and the realizability of the present results in experiments. In the present results we considered only the simplest domain, that of a triple periodic geometry, and we should give a word of caution in extrapolating them to domains with no-slip boundary conditions. In the presence of no-slip boundaries, rotation will introduce Ekman layers (Ekman 1905) that can

lead to large-scale drag effects (Caldwell, Van Atta & Helland 1972; Howroyd & Slawson 1975; Zavala Sansón, van Heijst & Backx 2001; Sous, Sommeria & Boyer 2013), altering in part the energy balance. Nonetheless, we do believe that in a carefully prepared experimental set-up where these effects are accounted for some of the presently observed phenomena would carry over to no-slip boundary conditions. In particular, it would be interesting to investigate the transition to the rotating condensate regime from 3D turbulence that displayed such rich behaviour. The high numerical cost of 3D simulations in this regime limits our runs to relatively short times, and does not allow us to study in detail their statistical behaviour. Experiments where long time series are easily attainable can then address this issue.

Acknowledgements

The authors would like to acknowledge various discussions with S. Fauve and the nonlinear physics group at ENS. This work was granted access to the HPC resources of MesoPSL financed by the Region Ile de France and the project Equip@Meso (reference ANR-10-EQPX-29-01) of the program Investissements d'Avenir, supervised by the Agence Nationale pour la Recherche, and the HPC resources of GENCI-TGCC-CURIE and GENCI-CINES-OCCIGEN (Project nos. x2015056421, x2016056421 and A0010506421) where the present numerical simulations have been performed.

REFERENCES

ALEXAKIS, A. 2011 Two-dimensional behavior of three-dimensional magnetohydrodynamic flow with a strong guiding field. *Phys. Rev.* E **84** (5), 056330.

ALEXAKIS, A. 2015 Rotating Taylor–Green flow. *J. Fluid Mech.* **769**, 46–78.

BAROUD, C. N., PLAPP, B. B., SHE, Z.-S. & SWINNEY, H. L. 2002 Anomalous self-similarity in a turbulent rapidly rotating fluid. *Phys. Rev. Lett.* **88** (11), 114501.

BAROUD, C. N., PLAPP, B. B., SWINNEY, H. L. & SHE, Z.-S. 2003 Scaling in three-dimensional and quasi-two-dimensional rotating turbulent flows. *Phys. Fluids* **15** (8), 2091–2104.

BARTELLO, P., METAIS, O. & LESIEUR, M. 1994 Coherent structures in rotating three-dimensional turbulence. *J. Fluid Mech.* **273**, 1–29.

BENAVIDES, S. J. & ALEXAKIS, A. 2017 Critical transitions in thin layer turbulence. *J. Fluid Mech.* **822**, 364–385.

BIFERALE, L., BONACCORSO, F., MAZZITELLI, I. M., VAN HINSBERG, M. A. T., LANOTTE, A. S., MUSACCHIO, S., PERLEKAR, P. & TOSCHI, F. 2016 Coherent structures and extreme events in rotating multiphase turbulent flows. *Phys. Rev.* X **6** (4), 041036.

BOFFETTA, G., DE LILLO, F., MAZZINO, A. & MUSACCHIO, S. 2011 A flux loop mechanism in two-dimensional stratified turbulence. *Europhys. Lett.* **95** (3), 34001.

VAN BOKHOVEN, L. J. A., CLERCX, H. J. H., VAN HEIJST, G. J. F. & TRIELING, R. R. 2009 Experiments on rapidly rotating turbulent flows. *Phys. Fluids* **21** (9), 096601.

BOUCHET, F. & SIMONNET, E. 2009 Random changes of flow topology in two-dimensional and geophysical turbulence. *Phys. Rev. Lett.* **102** (9), 094504.

BOUCHET, F. & VENAILLE, A. 2012 Statistical mechanics of two-dimensional and geophysical flows. *Phys. Rep.* **515** (5), 227–295.

BOUROUIBA, L. & BARTELLO, P. 2007 The intermediate rossby number range and two-dimensional–three-dimensional transfers in rotating decaying homogeneous turbulence. *J. Fluid Mech.* **587**, 139–161.

CALDWELL, D. R., VAN ATTA, C. W. & HELLAND, K. N. 1972 A laboratory study of the turbulent Ekman layer. *Geophys. Astrophys. Fluid Dyn.* **3** (1), 125–160.

CAMPAGNE, A., GALLET, B., MOISY, F. & CORTET, P.-P. 2014 Direct and inverse energy cascades in a forced rotating turbulence experiment. *Phys. Fluids* **26** (12), 125112.

CAMPAGNE, A., GALLET, B., MOISY, F. & CORTET, P.-P. 2015 Disentangling inertial waves from eddy turbulence in a forced rotating-turbulence experiment. *Phys. Rev.* E **91** (4), 043016.

CAMPAGNE, A., MACHICOANE, N., GALLET, B., CORTET, P.-P. & MOISY, F. 2016 Turbulent drag in a rotating frame. *J. Fluid Mech.* **794**, R5.

CELANI, A., MUSACCHIO, S. & VINCENZI, D. 2010 Turbulence in more than two and less than three dimensions. *Phys. Rev. Lett.* **104** (18), 184506.

CHEN, Q., CHEN, S., EYINK, G. L. & HOLM, D. D. 2005 Resonant interactions in rotating homogeneous three-dimensional turbulence. *J. Fluid Mech.* **542**, 139–164.

CLARK DI LEONI, P. & MININNI, P. D. 2016 Quantifying resonant and near-resonant interactions in rotating turbulence. *J. Fluid Mech.* **809**, 821–842.

COURANT, R., FRIEDRICHS, K. & LEWY, H. 1928 Über die partiellen Differenzengleichungen der Mathematischen. *Physik. Math. Ann.* **100**, 32–74.

DALLAS, V. & TOBIAS, S. M. 2016 Forcing-dependent dynamics and emergence of helicity in rotating turbulence. *J. Fluid Mech.* **798**, 682–695.

DEUSEBIO, E., BOFFETTA, G., LINDBORG, E. & MUSACCHIO, S. 2014 Dimensional transition in rotating turbulence. *Phys. Rev.* E **90** (2), 023005.

DICKINSON, S. C. & LONG, R. R. 1983 Oscillating-grid turbulence including effects of rotation. *J. Fluid Mech.* **126**, 315–333.

DURAN-MATUTE, M., FLÓR, J.-B., GODEFERD, F. S. & JAUSE-LABERT, C. 2013 Turbulence and columnar vortex formation through inertial-wave focusing. *Phys. Rev.* E **87** (4), 041001.

EKMAN, V. W. 1905 On the influence of the earth\'s rotation on ocean currents. *Ark. Mat. Astron. Fys.* **2**, 1–53.

FALKOVICH, G. & KRITSUK, A. G. 2017 How vortices and shocks provide for a flux loop in two-dimensional compressible turbulence. *Phys. Rev. Fluids* **2** (9), 092603.

FAVIER, B., GODEFERD, F. S. & CAMBON, C. 2010 On space and time correlations of isotropic and rotating turbulence. *Phys. Fluids* **22** (1), 015101.

FAVIER, B., SILVERS, L. J. & PROCTOR, M. R. E. 2014 Inverse cascade and symmetry breaking in rapidly rotating Boussinesq convection. *Phys. Fluids* **26** (9), 096605.

FRISHMAN, A., LAURIE, J. & FALKOVICH, G. 2017 Jets or vortices what flows are generated by an inverse turbulent cascade? *Phys. Rev. Fluids* **2** (3), 032602.

GALLET, B. 2015 Exact two-dimensionalization of rapidly rotating large-Reynolds-number flows. *J. Fluid Mech.* **783**, 412–447.

GALLET, B., CAMPAGNE, A., CORTET, P.-P. & MOISY, F. 2014 Scale-dependent cyclone–anticyclone asymmetry in a forced rotating turbulence experiment. *Phys. Fluids* **26** (3), 035108.

GALLET, B. & YOUNG, W. R. 2013 A two-dimensional vortex condensate at high Reynolds number. *J. Fluid Mech.* **715**, 359–388.

GALTIER, S. 2003 Weak inertial-wave turbulence theory. *Phys. Rev.* E **68** (1), 015301.

GODEFERD, F. S. & LOLLINI, L. 1999 Direct numerical simulations of turbulence with confinement and rotation. *J. Fluid Mech.* **393**, 257–308.

GREENSPAN, H. P. 1968 *The Theory of Rotating Fluids*. Cambridge University Press.

GUERVILLY, C. & HUGHES, D. W. 2017 Jets and large-scale vortices in rotating Rayleigh–Bénard convection. *Phys. Rev. Fluids* **2** (11), 113503.

GUERVILLY, C., HUGHES, D. W. & JONES, C. A. 2014 Large-scale vortices in rapidly rotating Rayleigh–Bérnard convection. *J. Fluid Mech.* **758**, 407–435.

HOPFINGER, E. J., BROWAND, F. K. & GAGNE, Y. 1982 Turbulence and waves in a rotating tank. *J. Fluid Mech.* **125**, 505–534.

HOPFINGER, E. J. & HEIJST, G. J. F. V. 1993 Vortices in rotating fluids. *Annu. Rev. Fluid Mech.* **25** (1), 241–289.

HOUGH, S. S. 1897 On the application of harmonic analysis to the dynamical theory of the tides. Part I. On Laplace's 'Oscillations of the first species', and on the dynamics of ocean currents. *Phil. Trans. R. Soc. Lond.* A **189**, 201–257.

HOWROYD, G. C. & SLAWSON, P. R. 1975 The characteristics of a laboratory produced turbulent Ekman layer. *Boundary-Layer Meteorol.* **8** (2), 201–219.

IBBETSON, A. & TRITTON, D. J. 1975 Experiments on turbulence in a rotating fluid. *J. Fluid Mech.* **68** (4), 639–672.

ISHIHARA, T., MORISHITA, K., YOKOKAWA, M., UNO, A. & KANEDA, Y. 2016 Energy spectrum in high-resolution direct numerical simulations of turbulence. *Phys. Rev. Fluids* **1** (8), 082403.

JULIEN, K., KNOBLOCH, E. & PLUMLEY, M. 2018 Impact of domain anisotropy on the inverse cascade in geostrophic turbulent convection. *J. Fluid Mech.* **837**.

KANEDA, Y., ISHIHARA, T., YOKOKAWA, M., ITAKURA, K. & UNO, A. 2003 Energy dissipation rate and energy spectrum in high resolution direct numerical simulations of turbulence in a periodic box. *Phys. Fluids* **15** (2), L21–L24.

KOLMOGOROV, A. N. 1941 The local structure of turbulence in incompressible viscous fluid for very large Reynolds number. *Proc. USSR Acad. Sci.* **30**, 299303.

KRAICHNAN, R. H. 1967 Inertial ranges in two-dimensional turbulence. *Tech. Rep.* DTIC Document.

KUNNEN, R. P., OSTILLA-MÓNICO, R., VAN DER POEL, E. P., VERZICCO, R. & LOHSE, D. 2016 Transition to geostrophic convection: the role of the boundary conditions. *J. Fluid Mech.* **799**, 413–432.

DI LEONI, P. C., COBELLI, P. J. & MININNI, P. D. 2015 The spatio-temporal spectrum of turbulent flows. *Euro. Phys. J.* E **38** (12), 136.

MACHICOANE, N., MOISY, F. & CORTET, P.-P. 2016 Two-dimensionalization of the flow driven by a slowly rotating impeller in a rapidly rotating fluid. *Phys. Rev. Fluids* **1**, 073701.

MARINO, R., MININNI, P. D., ROSENBERG, D. & POUQUET, A. 2013 Inverse cascades in rotating stratified turbulence: fast growth of large scales. *Europhys. Lett.* **102** (4), 44006.

MARINO, R., POUQUET, A. & ROSENBERG, D. 2015 Resolving the paradox of oceanic large-scale balance and small-scale mixing. *Phys. Rev. Lett.* **114** (11), 114504.

MININNI, P. D., ALEXAKIS, A. & POUQUET, A. 2009 Scale interactions and scaling laws in rotating flows at moderate Rossby numbers and large Reynolds numbers. *Phys. Fluids* **21** (1), 015108.

MININNI, P. D. & POUQUET, A. 2010 Rotating helical turbulence. I. Global evolution and spectral behavior. *Phys. Fluids* **22** (3), 035105.

MININNI, P. D., ROSENBERG, D., REDDY, R. & POUQUET, A. 2011 A hybrid MPI–OPENMP scheme for scalable parallel pseudospectral computations for fluid turbulence. *Parallel Comput.* **37** (6), 316–326.

MISHRA, P. K., HERAULT, J., FAUVE, S. & VERMA, M. K. 2015 Dynamics of reversals and condensates in two-dimensional Kolmogorov flows. *Phys. Rev.* E **91** (5), 053005.

MOISY, F., MORIZE, C., RABAUD, M. & SOMMERIA, J. 2011 Decay laws, anisotropy and cyclone–anticyclone asymmetry in decaying rotating turbulence. *J. Fluid Mech.* **666**, 5–35.

MORIZE, C. & MOISY, F. 2006 Energy decay of rotating turbulence with confinement effects. *Phys. Fluids* **18** (6), 065107.

NAZARENKO, S. 2011 *Wave Turbulence*, vol. 825. Springer Science & Business Media.

PEDLOSKY, J. 1987 *Geophysical Fluid Dynamics*. Springer.

PLUMLEY, M., JULIEN, K., MARTI, P. & STELLMACH, S. 2016 The effects of Ekman pumping on quasi-geostrophic Rayleigh–Bénard convection. *J. Fluid Mech.* **803**, 51–71.

POUQUET, A. & MARINO, R. 2013 Geophysical turbulence and the duality of the energy flow across scales. *Phys. Rev. Lett.* **111** (23), 234501.

POUQUET, A., SEN, A., ROSENBERG, D., MININNI, P. D. & BAERENZUNG, J. 2013 Inverse cascades in turbulence and the case of rotating flows. *Phys. Scr.* **2013** (T155), 014032.

PROUDMAN, J. 1916 On the motion of solids in a liquid possessing vorticity. *Phil. Trans. R. Soc. Lond.* A **92**, 408–424.

RICHARDSON, L. F. 1926 Atmospheric diffusion shown on a distance-neighbour graph. *Proc. R. Soc. Lond.* A **110** (756), 709–737.

ROBERTS, G. O. 1972 Dynamo action of fluid motions with two-dimensional periodicity. *Phil. Trans. R. Soc. Lond.* A **271** (1216), 411–454.

RUBIO, A. M., JULIEN, K., KNOBLOCH, E. & WEISS, J. B. 2014 Upscale energy transfer in three-dimensional rapidly rotating turbulent convection. *Phys. Rev. Lett.* **112**, 144501.

RUPPERT-FELSOT, J. E., PRAUD, O., SHARON, E. & SWINNEY, H. L. 2005 Extraction of coherent structures in a rotating turbulent flow experiment. *Phys. Rev.* E **72** (1), 016311.

SCOTT, J. F. 2014 Wave turbulence in a rotating channel. *J. Fluid Mech.* **741**, 316–349.

SEN, A., MININNI, P. D., ROSENBERG, D. & POUQUET, A. 2012 Anisotropy and nonuniversality in scaling laws of the large-scale energy spectrum in rotating turbulence. *Phys. Rev.* E **86** (3), 036319.

SESHASAYANAN, K. & ALEXAKIS, A. 2016 Critical behavior in the inverse to forward energy transition in two-dimensional magnetohydrodynamic flow. *Phys. Rev.* E **93** (1), 013104.

SESHASAYANAN, K., BENAVIDES, S. J. & ALEXAKIS, A. 2014 On the edge of an inverse cascade. *Phys. Rev.* E **90** (5), 051003.

SESHASAYANAN, K., DALLAS, V. & ALEXAKIS, A. 2017 The onset of turbulent rotating dynamos at the low magnetic Prandtl number limit. *J. Fluid Mech.* **822**, R3.

SHATS, M. G., XIA, H., PUNZMANN, H. & FALKOVICH, G. 2007 Suppression of turbulence by self-generated and imposed mean flows. *Phys. Rev. Lett.* **99** (16), 164502.

SMITH, L. M., CHASNOV, J. R. & WALEFFE, F. 1996 Crossover from two-to three-dimensional turbulence. *Phys. Rev. Lett.* **77** (12), 2467.

SMITH, L. M. & WALEFFE, F. 1999 Transfer of energy to two-dimensional large scales in forced, rotating three-dimensional turbulence. *Phys. Fluids* **11**, 1608–1622.

SMITH, L. M. & YAKHOT, V. 1994 Finite-size effects in forced two-dimensional turbulence. *J. Fluid Mech.* **274**, 115–138.

SOUS, D., SOMMERIA, J. & BOYER, D. L. 2013 Friction law and turbulent properties in a laboratory Ekman boundary layer. *Phys. Fluids* **25** (4), 046602.

SOZZA, A., BOFFETTA, G., MURATORE-GINANNESCHI, P. & MUSACCHIO, S. 2015 Dimensional transition of energy cascades in stably stratified forced thin fluid layers. *Phys. Fluids* **27** (3), 035112.

SREENIVASAN, B. & DAVIDSON, P. A. 2008 On the formation of cyclones and anticyclones in a rotating fluid. *Phys. Fluids* **20** (8), 085104.

SREENIVASAN, K. R. 1984 On the scaling of the turbulence energy dissipation rate. *Phys. Fluids* **27** (5), 1048–1051.

STAPLEHURST, P. J., DAVIDSON, P. A. & DALZIEL, S. B. 2008 Structure formation in homogeneous freely decaying rotating turbulence. *J. Fluid Mech.* **598**, 81–105.

STELLMACH, S., LISCHPER, M., JULIEN, K., VASIL, G., CHENG, J. S., RIBEIRO, A., KING, E. M. & AURNOU, J. M. 2014 Approaching the asymptotic regime of rapidly rotating convection: boundary layers versus interior dynamics. *Phys. Rev. Lett.* **113** (25), 254501.

SUGIHARA, Y., MIGITA, M. & HONJI, H. 2005 Orderly flow structures in grid-generated turbulence with background rotation. *Fluid Dyn. Res.* **36**, 23–34.

TAYLOR, G. I. 1917 Motion of solids in fluids when the flow is not irrotational. *Proc. R. Soc. Lond.* A **93**, 99–113.

THIELE, M. & MÜLLER, W.-C. 2009 Structure and decay of rotating homogeneous turbulence. *J. Fluid Mech.* **637**, 425.

TSANG, Y. K. & YOUNG, W. R. 2009 Forced-dissipative two-dimensional turbulence: a scaling regime controlled by drag. *Phys. Rev.* E **79** (4), 045308.

VALENTE, P. C. & DALLAS, V. 2017 Spectral imbalance in the inertial range dynamics of decaying rotating turbulence. *Phys. Rev.* E **95** (2), 023114.

VAN BOKHOVEN, L. J. A., CAMBON, C., LIECHTENSTEIN, L., GODEFERD, F. S. & CLERCX, H. J. H. 2008 Refined vorticity statistics of decaying rotating three-dimensional turbulence. *J. Turbul.* **9** (N6).

WEEKS, E. R., TIAN, Y., URBACH, J. S., IDE, K., SWINNEY, H. L. & GHIL, M. 1997 Transitions between blocked and zonal flows in a rotating annulus with topography. *Science* **278** (5343), 1598–1601.

XIA, H., PUNZMANN, H., FALKOVICH, G. & SHATS, M. G. 2008 Turbulence-condensate interaction in two dimensions. *Phys. Rev. Lett.* **101** (19), 194504.

YAROM, E. & SHARON, E. 2014 Experimental observation of steady inertial wave turbulence in deep rotating flows. *Nat. Phys.* **10** (7), 510–514.

YAROM, E., VARDI, Y. & SHARON, E. 2013 Experimental quantification of inverse energy cascade in deep rotating turbulence. *Phys. Fluids* **25** (8), 085105.

YEUNG, P. K. & ZHOU, Y. 1998 Numerical study of rotating turbulence with external forcing. *Phys. Fluids* **10** (11), 2895–2909.

YOKOYAMA, N. & TAKAOKA, M. 2017 Hysteretic transitions between quasi-two-dimensional flow and three-dimensional flow in forced rotating turbulence. *Phys. Rev. Fluids* **2** (9), 092602.

YOSHIMATSU, K., MIDORIKAWA, M. & KANEDA, Y. 2011 Columnar eddy formation in freely decaying homogeneous rotating turbulence. *J. Fluid Mech.* **677**, 154–178.

ZAVALA SANSÓN, L., VAN HEIJST, G. J. F. & BACKX, N. A. 2001 Ekman decay of a dipolar vortex in a rotating fluid. *Phys. Fluids* **13** (2), 440–451.

ZEMAN, O. 1994 A note on the spectra and decay of rotating homogeneous turbulence. *Phys. Fluids* **6** (10), 3221–3223.